

## Article

# Screening $Ba_{0.9}A_{0.1}MnO_3$ and $Ba_{0.9}A_{0.1}Mn_{0.7}Cu_{0.3}O_3$ (A = Mg, Ca, Sr, Ce, La) Sol-Gel Synthesised Perovskites as GPF Catalysts

Nawel Ghezali, Álvaro Díaz Verde  and María José Illán Gómez \* 

MCMA Group, Inorganic Chemistry Department and Institute of Materials of the University of Alicante (IUMA), Faculty of Sciences, University of Alicante, 03690 Alicante, Spain; ghezalinawel34@gmail.com (N.G.); alvaro.diaz@ua.es (Á.D.V.)

\* Correspondence: illan@ua.es

**Abstract:**  $Ba_{0.9}A_{0.1}MnO_3$  (BM-A) and  $Ba_{0.9}A_{0.1}Mn_{0.7}Cu_{0.3}O_3$  (BMC-A) (A = Mg, Ca, Sr, Ce, La) perovskite-type mixed oxides were synthesised, characterised, and used for soot oxidation in simulated Gasoline Direct Injection (GDI) engine exhaust conditions. The samples have been obtained by the sol-gel method in an aqueous medium and deeply characterised. The characterization results indicate that the partial substitution of Ba by A metal in  $BaMnO_3$  (BM) and  $BaMn_{0.7}Cu_{0.3}O_3$  (BMC) perovskites: (i) favours the hexagonal structure of perovskite; (ii) improves the reducibility and the oxygen desorption during Temperature-Programmed Desorption ( $O_2$ -TPD) tests and, consequently, the oxygen mobility; (iii) maintains the amount of oxygen vacancies and of Mn(IV) and Mn(III) oxidation states, being Mn(IV) the main one; and (iv) for  $Ba_{0.9}A_{0.1}Mn_{0.7}Cu_{0.3}O_3$  (BMC-A) series, copper is partially incorporated into the structure. The soot conversion data reveal that  $Ba_{0.9}La_{0.1}Mn_{0.7}Cu_{0.3}O_3$  (BMC-La) is the most active catalyst in an inert (100% He) reaction atmosphere, as it presents the highest amount of copper on the surface, and that  $Ba_{0.9}Ce_{0.1}Mn_{0.7}Cu_{0.3}O_3$  (BM-Ce) is the best one if a low amount of  $O_2$  (1%  $O_2$  in He) is present, as it combines the highest emission of oxygen with the good redox properties of Ce(IV)/Ce(III) and Mn(IV)/Mn(III) pairs.

**Keywords:** perovskite; cerium; lanthanum; calcium; magnesium; strontium; copper; soot oxidation; GDI engines



**Citation:** Ghezali, N.; Díaz Verde, Á.; Illán Gómez, M.J. Screening  $Ba_{0.9}A_{0.1}MnO_3$  and  $Ba_{0.9}A_{0.1}Mn_{0.7}Cu_{0.3}O_3$  (A = Mg, Ca, Sr, Ce, La) Sol-Gel Synthesised Perovskites as GPF Catalysts. *Materials* **2023**, *16*, 6899. <https://doi.org/10.3390/ma16216899>

Academic Editor: Aleksey Zarkov

Received: 28 September 2023

Revised: 20 October 2023

Accepted: 25 October 2023

Published: 27 October 2023



**Copyright:** © 2023 by the authors. Licensee MDPI, Basel, Switzerland. This article is an open access article distributed under the terms and conditions of the Creative Commons Attribution (CC BY) license (<https://creativecommons.org/licenses/by/4.0/>).

## 1. Introduction

Nowadays, the accumulation in the atmosphere of pollutants generated by automobile engines is one of the main environmental problems due to their negative effects. During the combustion process, gasoline and diesel engines emit harmful compounds such as carbon monoxide, nitrogen oxides, and particulate matter (PM) that seriously affect the air quality [1]. These primary pollutants react with other atmospheric compounds to form secondary pollutants, such as, among others, ground-level ozone, which stands out for being harmful to plants and causing respiratory issues in humans. GDI engines present high fuel efficiency and low  $CO_2$  emissions but generate a high amount of PM, especially with a diameter lower than 10  $\mu m$ , which is the most dangerous one as it can deeply penetrate into the organism (lungs, bloodstream, etc.) [2]. As a result, the European Commission (by the European Green Deal's Zero Pollution Action Plan [3]) established the 2030 target, which consists of lowering the number of particulate matter with a diameter of 2.5  $\mu m$  (PM<sub>2.5</sub>) by at least 44% of 2005 levels. To deal with this problem, gasoline particulate filters (GPFs) are being used in GDI engine vehicles, which must undergo routine regeneration to avoid soot accumulation in the inner channel. On the other hand, three-way catalysts (TWCs) have been employed to remove the gaseous pollutants from gasoline engines since the 1980s. Thus, both TWCs and GPFs are essential after-treatment devices for GDI engines in order to meet the Euro 6 limits [4]. In this context, catalysts for soot removal at low temperatures and at low oxygen (or zero) partial pressures are highly demanded for GPF

devices [5]. Until now, noble metal-based catalysts were the most commonly employed formulations for GDI soot removal, especially those composed by Pt. However, noble metals are scarce and expensive [6–8], making it mandatory to look for alternative and more economically accessible formulations. Recently, ceria-based mixed oxides have been proposed as promising catalysts due to their oxygen storage properties and the versatility of Ce to modify its oxidation state [9].

In this context, perovskite-type mixed oxides ( $ABO_3$ ) are also considered potential catalytic formulations for soot oxidation, as they exhibit intriguing and adjustable physico-chemical properties that could be improved by using different strategies, such as, among others, the modification of the composition by the partial substitution of A and/or B cations [10–13]. In general, transition metals (Fe, Co, Mn, Cr, Cu, V, etc.) are usually located in the B position, while lanthanide and/or alkaline earth metals (Sr, Ca, Ba, etc.) typically occupy the A position [10,14]. Because of the doping with A and/or B cations with different sizes and oxidation states, the redox properties, the generation of oxygen vacancies and the oxygen mobility of perovskites can be greatly improved [10,15]. Additionally, the doping could also modify the electronic structure and, consequently, the semiconductor properties, making these solids good candidates for several catalytic and electrocatalytic applications, such as the  $CO_2$  reduction reaction ( $CO_2RR$ ) [16–18], the oxygen reduction reaction (ORR) [19], the oxygen evolution reaction (OER) [20], and some photocatalytic processes [19,21,22]. Thus, in previous studies, the authors determined that the partial substitution of iron by copper in a  $BaFe_{1-x}Cu_xO_3$  catalyst series ( $x = 0, 0.1, 0.3, \text{ and } 0.4$ ) modifies the catalytic performance for soot oxidation under GDI and diesel engine exhaust conditions [23,24]. These perovskites catalyzed the oxidation of soot in both exhaust conditions that are in the presence of  $NO_2$  (diesel engines) and the 1%  $O_2$  (“fuel cut” stage of GDI engine exhaust).  $BaFeO_3$  perovskite was the most active catalyst, whose performance was mainly related to the lattice oxygen mobility, which decreased with copper content.

On the other hand, it is well established that  $AMnO_3$  perovskites, due to their redox properties related to the electronic configuration of Mn(III) and Mn(IV) [25–27], are active catalysts for oxidation reactions. Moreover, Mn(III) presents the Jahn–Teller effect, which is a distortion that provokes some structural defects that generate active sites for oxidation reactions [28–30]. Thus, the presence of these two oxidation states, especially an enriched Mn(IV) surface, increases the oxygen mobility and, consequently, the catalytic activity for the oxidation of soot [31]. In fact, in a previous work, the authors used  $BaMnO_3$  and  $BaMn_{1-x}Cu_xO_3$  mixed oxides with a perovskite-like structure (obtained by employing various synthesis methods that allow particular chemical and physical properties) as feasible catalysts for GPF systems [31]. The results obtained for soot removal in simulated GDI engine exhaust conditions (i.e., low percentage of oxygen) reveal that, on the one hand, the presence of oxygen vacancies is required to adsorb and activate oxygen, and, on the other hand, a labile Mn(IV)/Mn(III) redox pair is needed to dissociate the adsorbed oxygen. Thus, the coexistence of both properties allows the transport of the activated oxygen towards the soot.

Considering these conclusions, the aim of this work is the synthesis by the sol-gel method of two series of barium manganese perovskite-type mixed oxides in which 10% of barium has been replaced (i.e.,  $Ba_{0.9}A_{0.1}MnO_3$  and  $Ba_{0.9}A_{0.1}Mn_{0.7}Cu_{0.3}O_3$ , where  $A = Ca, Sr, Mg, Ce, \text{ or } La$ ). These samples will be tested as catalysts for GPFs to be used for soot removal in simulated GDI engine exhaust conditions.

## 2. Materials and Methods

### 2.1. Synthesis of Catalyst

The sol-gel method adapted to aqueous medium [32–34] was used for the synthesis of the two series ( $Ba_{0.9}A_{0.1}MnO_3$  and  $Ba_{0.9}A_{0.1}Mn_{0.7}Cu_{0.3}O_3$ ) of samples. The metal precursors used are the following: barium acetate ( $Ba(CH_3COO)_2$ , Sigma-Aldrich, St. Louis, MO, USA 99.0% purity), calcium nitrate tetrahydrate ( $Ca(NO_3)_2 \cdot 4H_2O$ , Sigma-Aldrich, 99.0% purity), lanthanum(III) nitrate hydrate ( $La(NO_3)_3 \cdot H_2O$ , Sigma-Aldrich,

99.0% purity), magnesium nitrate hexahydrate ( $\text{Mg}(\text{NO}_3)_2 \cdot 6\text{H}_2\text{O}$ , Sigma-Aldrich, 99.0% purity), cerium(III) nitrate hexahydrate ( $\text{Ce}(\text{NO}_3)_3 \cdot 6\text{H}_2\text{O}$ , Sigma-Aldrich, 99.0% purity), strontium nitrate ( $\text{Sr}(\text{NO}_3)_2$ , Sigma-Aldrich, 99.0% purity), copper(II) nitrate trihydrate ( $\text{Cu}(\text{NO}_3)_2 \cdot 3\text{H}_2\text{O}$ , Panreac, Castellar del Vallès, Spain, 99.0% purity), and manganese(II) nitrate tetrahydrate ( $\text{Mn}(\text{NO}_3)_2 \cdot 4\text{H}_2\text{O}$ , Sigma-Aldrich, 99.0% purity). Additionally, citric acid ( $\text{C}_6\text{H}_8\text{O}_7$ , Sigma-Aldrich, 99.0% purity) has been employed as a complexing agent (using a citric acid/Ba ratio of 2), and EDTA (Sigma-Aldrich, 98.5% purity) has also been added as a chelating agent (EDTA/Ba = 2) for the synthesis of the  $\text{BaMnO}_3$  reference sample to avoid the precipitation of metal precursors. To obtain the gel, citric acid was dissolved in 40 mL of distilled water at 60 °C, and then the metal precursors, in the same order in which the metals appear in the perovskite formulae, are added. In the case of the  $\text{BaMnO}_3$  reference sample, EDTA is incorporated into the dissolution before the metal precursors, and, finally, citric acid is included. After that, the solution was stirred at 65 °C for 5 h. Throughout the process, the pH was maintained at 8.5 by adding an ammonia solution (Panreac, 30.0 wt%). Then, the gel was dried at 90 °C for 48 h, and the resulting powder was calcined at 850 °C for 6 h.

## 2.2. Characterization

For sample characterization, the following techniques were employed.

The elemental composition was obtained by Inductively Coupled Plasma Optical Emission Spectroscopy (ICP-OES) on a Perkin-Elmer device model Optimal 4300 DV (Waltham, MA, USA). For each experiment, 10 mg of catalyst was dissolved in a mixture of 5 mL of aqua regia and 10 mL of distilled water.

The textural properties were obtained by  $\text{N}_2$  adsorption (at  $-196$  °C) in an Autosorb-6B device (Quantachrome, Anton Paar Austria GmbH, Graz, Austria). Before the adsorption experiments, degassification at 250 °C for 4 h was carried out.

X-ray Diffraction (XRD) was used for determining the crystalline structure, using the XRD patterns recorded (in a Bruker D8-Advance device, Billerica, MA, USA) between 20° and 80° 2 $\theta$  angles (step rate of 0.4°/min) and using  $\text{Cu K}\alpha$  (0.15418 nm) radiation.

Surface chemistry composition was obtained by X-ray photoelectron spectroscopy (XPS) in a K-Alpha photoelectron spectrometer device (Thermo-Scientific, Waltham, MA, USA) with an  $\text{Al K}\alpha$  (1486.7 eV) radiation source. To obtain XPS spectra, the pressure of the analysis chamber was held at  $5 \times 10^{-10}$  mbar. The binding energy (BE) and kinetic energy (KE) scales were adjusted by setting the C 1s transition to 284.6 eV, and the BE and KE values were determined with the peak-fit software of the spectrometer (Thermo Avantage v5.9929).

Temperature-Programmed Reduction with  $\text{H}_2$  ( $\text{H}_2$ -TPR) in a Pulse Chemisorb 2705 (from Micromeritics, Norcross, GA, USA) provided by a Thermal Conductivity Detector (TCD) was used to estimate the reducibility of samples. For the tests, 30 mg of sample, heated at 10 °C/min from 25 °C to 1000 °C in a 5%  $\text{H}_2$ /Ar atmosphere (40 mL/min), was used. A CuO reference sample was employed for the quantification of  $\text{H}_2$  consumption.

Oxygen Temperature-Programmed Desorption ( $\text{O}_2$ -TPD) experiments were performed in a Thermal Gravimetric Mass Spectrometry (TG-MS) device (Q-600-TA and Thermostat from Balzers Instruments (Balzers, Liechtenstein), respectively). Sixteen milligrams of sample (heated at 10 °C/min from room temperature to 950 °C under a 100 mL/min helium atmosphere) was used. Before the experiments, samples were preheated to 150 °C for 1 h for moisture removal. The 18, 28, 32, and 44  $m/z$  signals were recorded for the quantification of  $\text{H}_2\text{O}$ , CO,  $\text{O}_2$ , and  $\text{CO}_2$  evolved. The amount of oxygen was calculated based on a CuO reference sample.

## 2.3. Activity Tests

The soot oxidation tests (under simulated GDI engine exhaust conditions) were developed on the TG-MS device employed for  $\text{O}_2$ -TPD. Thus, 16 mg of a catalyst and soot mixture (soot:catalyst ratio of 1:8, using Printex-U as model soot in loose contact mode) was preheated at 150 °C (1 h) in a 1%  $\text{O}_2$ /He mixture (100 mL/min); subsequently, the

temperature was increased until 900 °C at 10 °C/min (soot-TPR). Two different reactant mixtures were employed: (i) 1% O<sub>2</sub>/He, which reproduces “fuel cuts” GDI engine exhaust conditions, and (ii) 100% He, which represents regular stoichiometric GDI engine operations [23,24,31].

The soot conversion and the selectivity to CO<sub>2</sub> percentages were calculated by these equations:

$$\text{Soot conversion (\%)} = \frac{\sum_0^t \text{CO}_2 + \text{CO}}{\sum_0^{\text{final}} (\text{CO}_2 + \text{CO})} \times 100 \quad (1)$$

$$\text{Selectivity to CO}_2 \text{ (\%)} = \frac{\text{CO}_2 \text{ total}}{(\text{CO}_2 + \text{CO})_{\text{total}}} \cdot 100 \quad (2)$$

where  $\sum_0^t (\text{CO}_2 + \text{CO})$  is the amount of CO<sub>2</sub> and CO generated at time  $t$ , while  $\sum_0^{\text{final}} (\text{CO}_2 + \text{CO})$  is the total amount of CO + CO<sub>2</sub> evolved during the experiment, coming from the oxidation of the total amount of soot.

### 3. Results and Discussion

#### 3.1. Characterization

##### 3.1.1. Ba<sub>0.9</sub>A<sub>0.1</sub>MnO<sub>3</sub> Series

The nomenclature for the mixed oxides is shown in Table 1, along with the specific surface area values (obtained by applying the Brunauer-Emmett-Teller (BET) equation to N<sub>2</sub> adsorption data), the A metal content (determined by ICP-OES), and some XRD data.

**Table 1.** Nomenclature, XRD data, metal content and BET surface area of BM-A catalysts.

| Nomenclature | Molecular Formula                                    | Specific Surface Area (m <sup>2</sup> /g) | A (wt%) | Intensity (a.u.) <sup>a</sup> | Average Crystal Size (nm) | Cell Parameters (Å) <sup>b</sup> |          |
|--------------|--|---|---------|-------------------------------|---------------------------|----------------------------------|----------|
|              |  |   |         |                               |                           | <i>a</i>                         | <i>c</i> |
| BM           | BaMnO <sub>3</sub>                                   | 3   | -       | 1154                          | 46                        | 5.7                              | 4.9      |
| BM-Ca        | Ba <sub>0.9</sub> Ca <sub>0.1</sub> MnO <sub>3</sub> | 11  | 1.6     | 1913                          | 25                        | 5.7                              | 4.8      |
| BM-La        | Ba <sub>0.9</sub> La <sub>0.1</sub> MnO <sub>3</sub> | 7   | 1.1     | 1562                          | 28                        | 5.7                              | 4.8      |
| BM-Mg        | Ba <sub>0.9</sub> Mg <sub>0.1</sub> MnO <sub>3</sub> | 7   | 4.2     | 2382                          | 28                        | 5.7                              | 4.8      |
| BM-Sr        | Ba <sub>0.9</sub> Sr <sub>0.1</sub> MnO <sub>3</sub> | 5   | 4.8     | 2382                          | 18                        | 5.6                              | 4.9      |
| BM-Ce        | Ba <sub>0.9</sub> Ce <sub>0.1</sub> MnO <sub>3</sub> | 10  | 1.3     | 1913                          | 22                        | 5.5                              | 5.0      |

<sup>a</sup> Corresponding to the main XRD hexagonal perovskite peak, <sup>b</sup> Calculated using the main XRD hexagonal perovskite peak.

The low surface areas presented in Table 1 suggest, as expected for perovskite-type mixed oxides [10], that all samples present low specific surface areas and extremely small porosity development that, according to K. Akinlolu [35], could be a consequence of the calcination conditions used in the synthesis (850 °C). Note that the calcination temperature used for synthesis was the minimum one needed to obtain the perovskite phase [36] because, if higher temperatures were used, larger crystal sizes would be obtained, thus promoting a decrease in the number of active sites [37]. On the other hand, ICP-OES data confirm that the mixed oxides contain almost all the amount of A metal supplied during the synthesis.

Figure 1a shows the XRD patterns of samples, including the raw BaMnO<sub>3</sub> (BM), obtained also by the sol-gel method. The hexagonal 2H-BaMnO<sub>3</sub> perovskite structure (PDF number: 026-0168, denoted by the ICDD, the International Centre of Diffraction Data) is the main crystalline phase for all samples [32]. This structure is formed by chains of face-sharing MnO<sub>6</sub> units rather than by corner-sharing MnO<sub>6</sub> units [32,36,38]. Note that the partial substitution of the A cation does not cause a significant change to the BaMnO<sub>3</sub> hexagonal perovskite structure, as the position of the main peak (shown in Figure 1b) and the values of the *a* and *c* cell parameters (included in Table 1) are similar to those shown by BM. However, the intensity of the main XRD peak of the hexagonal perovskite structure

is higher for all BM-A samples than for BM perovskite, suggesting that the addition of A metal promotes crystal growth during the calcination step. On the other hand,  $\text{Ba}_3\text{Mn}_2\text{O}_8$  and  $\text{MnO}_2$  (PDF numbers: 073-0997 and 024-0735, respectively) are detected as minority phases. The Williamson-Hall method [39] was used to determine the average crystallite size shown in Table 1, and a decrease is detected after the partial substitution of Ba by A metal, presenting BM-Sr the lowest value.

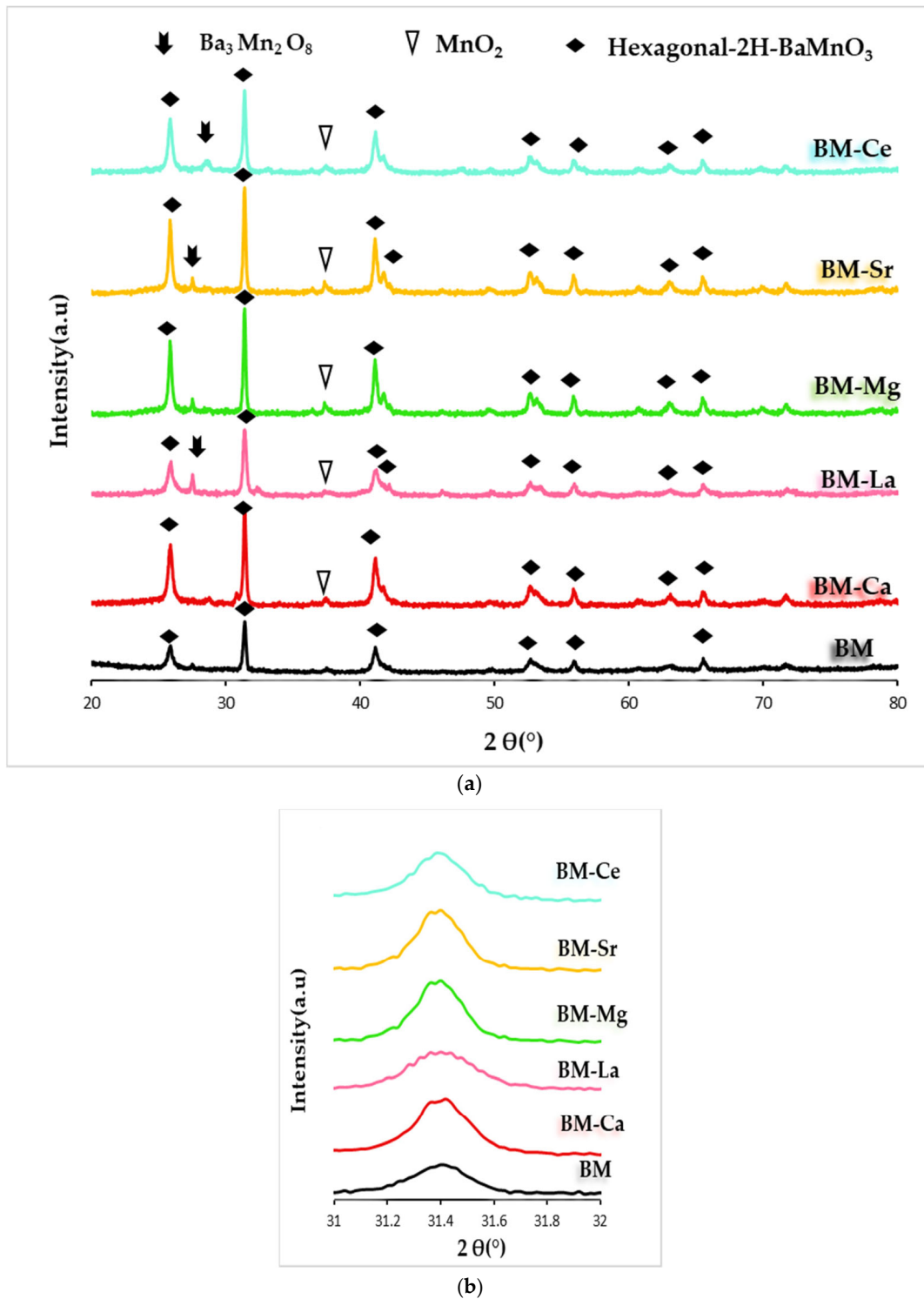


**Figure 1.** (a) XRD profiles of BM-A and BM catalysts, and (b) magnification corresponding to the hexagonal 2H-BaMnO<sub>3</sub> diffraction peak.



XPS gives information about the species present on the surface and Figure 2 shows the O 1s (a) and Mn 2p<sub>3/2</sub> (b) XPS spectra for BM and BM-A samples.

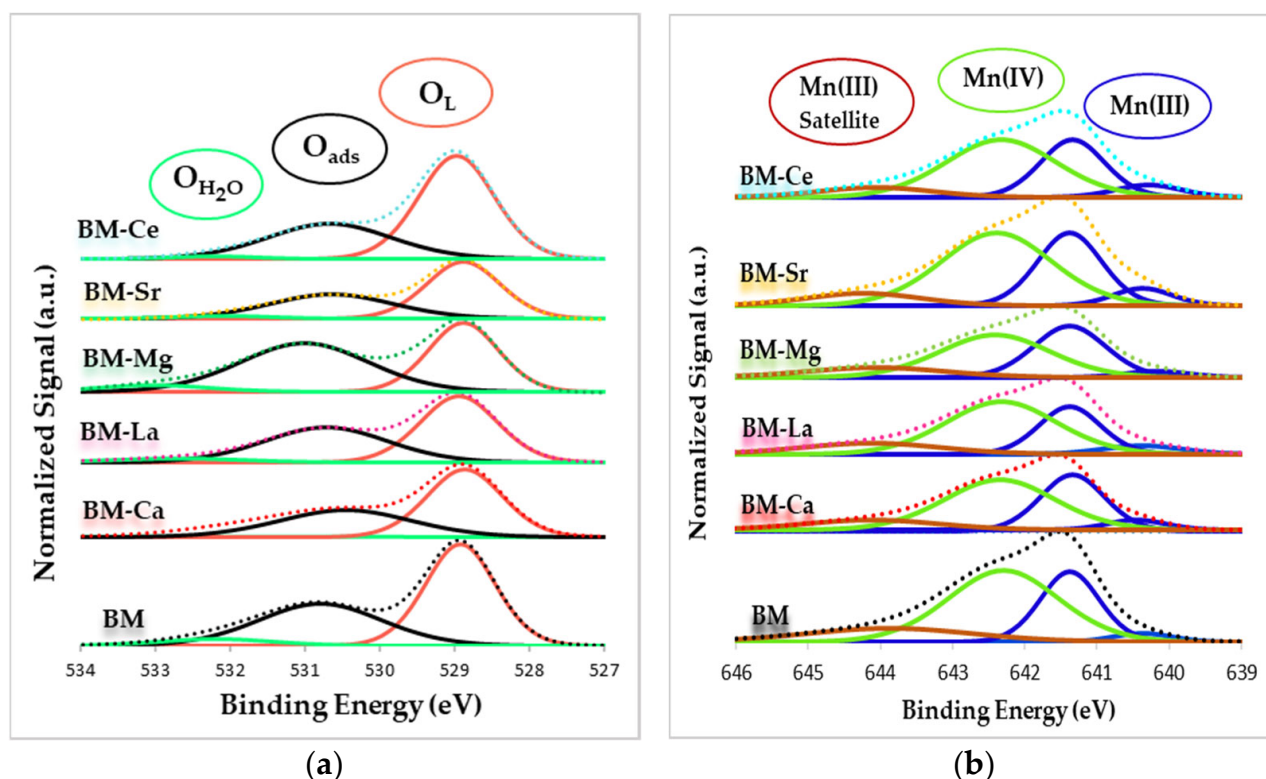


**Figure 2.** XPS spectra of BM-A and BM catalysts in the (a) O 1s and (b) Mn 2p<sub>3/2</sub> core levels regions.

In the O 1s XPS spectra, featured in Figure 2a, three different contributions are observed [40,41]: (i) at low binding energies, a sharp peak centered around 529 eV, which is attributed to lattice oxygen (the so-called “O<sub>L</sub>”), (ii) at intermediate binding energies (around 531 eV), a wide peak which corresponds to adsorbed oxygen species (named “O<sub>ads</sub>”), such as surface carbonate (CO<sub>3</sub><sup>2-</sup>), hydroxyl groups (OH<sup>-</sup>) and peroxide (O<sub>2</sub><sup>2-</sup>) or superoxide (O<sub>2</sub><sup>-</sup>) ions, and (iii) a peak at higher binding energies (532 eV) associated to chemisorbed water (labelled as “O<sub>H2O</sub>”). From these XPS spectra, the binding energies for the maximum of the O<sub>L</sub> and O<sub>ads</sub> deconvoluted bands have been obtained, which are included in Table 2, and these data indicate that the partial Ba replacement does not significantly affect the binding energy of the deconvoluted peak maxima. The O<sub>L</sub>/(Ba + Mn + A) ratio, calculated using the area under the O<sub>L</sub> peak and the areas under the signals associated with cations (Table 2), would reveal that surface oxygen vacancies exist if the O<sub>L</sub>/(Ba + Mn + A) XPS ratio is lower than the nominal one (1.5, calculated based on the chemical formulae of the perovskite) [32,40,42]. So, because all the XPS ratios are lower than 1.5, oxygen vacancies exist on the surface of all samples, and the partial replacement of Ba does not substantially change these values. The generation of oxygen surface vacancies [32,36,40], which is required to achieve the positive charge imbalance caused by Mn(III) (see next paragraph), is relevant in the soot oxidation reaction [42] because it allows the creation of the reactive oxygen species.

In the Mn 2p<sub>3/2</sub> XPS spectra shown in Figure 2b, the following contributions are detected: (i) Mn(III), located at around 641 eV; (ii) Mn(IV), found at approximately 642 eV; and (iii) the Mn(III) satellite peaks at ca 644 eV [32,42–45]. These spectra reveal that Mn(III) and Mn(IV) coexist on the surface. This fact, previously observed [32,36,45,46] for manganese-based perovskites, indicates that the Mn(II) precursor is being oxidized to Mn(III)/Mn(IV) to achieve electroneutrality on the surface. Note that on the surface of an ideal BaMnO<sub>3</sub> perovskite (considering the charges of barium (Ba<sup>2+</sup>) and oxygen (O<sup>2-</sup>))

ions), Mn(IV) species must be present to preserve the electroneutrality. However, as oxygen vacancies exist on the surface (as already demonstrated by O 1s transition data), Mn(III) should be present to compensate the negative charge deficiency. The Mn(IV)/Mn(III) ratio, calculated with the area of the deconvoluted XPS peaks and included in Table 2, features that Mn(IV) is the predominant oxidation state for all catalysts, as all the Mn(IV)/Mn(III) values are above 1. However, a decrease in the Mn(IV) amount is observed after partial substitution of Ba by A metal, being more significant for BM-Mg. As indicated in the introduction, the presence of both oxidation states is relevant, and it could be expected that, as it was observed in other studies focused on La-Mn and Ba-Mn perovskite-type catalysts [32,38,42,45,46], a surface enriched with Mn(IV) allows improved oxygen mobility, thus enhancing the catalytic activity.

**Table 2.** XPS data of BM and BM-A catalysts.

| Catalyst | B.E Max<br>Mn(III)<br>(eV) | B.E Max<br>Mn(VI)<br>(eV) | B.E Max<br>O <sub>L</sub><br>(eV) | B.E Max<br>O <sub>ads</sub><br>(eV) | $\frac{O_L}{(Ba + Mn + A)}$<br>(Nominal = 1.5) | $\frac{Mn(IV)}{Mn(III)}$ |
|----------|----------------------------|---------------------------|-----------------------------------|-------------------------------------|--|--------------------------|
| BM       | 641.4                      | 642.3                     | 528.9                             | 530.8                               | 1.0  | 1.7                      |
| BM-Ca    | 641.3                      | 642.3                     | 528.9                             | 530.5                               | 1.0  | 1.6                      |
| BM-La    | 641.4                      | 642.3                     | 529.0                             | 530.7                               | 1.0  | 1.6                      |
| BM-Mg    | 641.4                      | 642.3                     | 528.9                             | 531.0                               | 1.0  | 1.1                      |
| BM-Sr    | 641.4                      | 642.4                     | 528.9                             | 530.7                               | 1.1  | 1.4                      |
| BM-Ce    | 641.4                      | 642.4                     | 529.0                             | 530.7                               | 1.0  | 1.4                      |

Temperature-Programmed Reduction tests using hydrogen as a reducing agent (H<sub>2</sub>-TPR) allow estimating the reducibility and redox properties of samples. The H<sub>2</sub> consumption profiles for perovskites are determined by the oxidation state and redox properties of the B-site metal [30,45], and the number and sequence of these peaks are strongly dependent on their identity [10,38]. On the other hand, according to the literature, the metal at the A-site typically shows a unique oxidation state and is hardly reduced [10,47]. The H<sub>2</sub>-TPR profile for MnO<sub>2</sub>, used as a reference, presents two overlapping peaks at around 400 and 500 °C that correspond to the reduction of MnO<sub>2</sub>/Mn<sub>2</sub>O<sub>3</sub> to Mn<sub>3</sub>O<sub>4</sub> and of Mn<sub>3</sub>O<sub>4</sub> to MnO, respectively [48]. Usually [30,32,42,45,47], a multiple-step reduction was observed for the manganese-based samples, showing: (i) an intense peak centered between 400–600 °C, corresponding to the Mn(IV) and Mn(III) reduction to Mn(II); (ii) a small peak from 700 °C to 800 °C due to the oxygen species reduction; and (iii) a third peak with a maximum between 900 °C and 1000 °C, corresponding to the Mn(III) to Mn(II) reduction in the bulk [47]. The H<sub>2</sub>-TPR profiles of BM-A samples (Figure 3a) reveal that only for BM-La and BM-Mg, the higher reduction peak appears at lower temperatures than in BM, indicating an improvement in the redox properties. Based on the hydrogen consumption profiles shown in Figure 3a, the experimental hydrogen consumption per gram of sample has been calculated over the temperature range between 450 °C and 600 °C, and these data have been compared in Figure 3b with the theoretical hydrogen consumption calculated assuming a complete reduction of manganese, being as pure Mn(III) (blue line) or pure Mn(IV) (red line). Note that, for BM-A samples, the experimental H<sub>2</sub> consumptions are placed between both Mn(IV) and Mn(III) nominal values, being closer to Mn(III) for BM-Ca and to Mn(IV) for BM-Mg, as well as for raw BM. Thus, it seems that, as observed on the surface of catalysts (see XPS results), Mn(III)/Mn(IV) oxidation states are present in the bulk of all samples, and the predominant oxidation state is determined by the A metal.

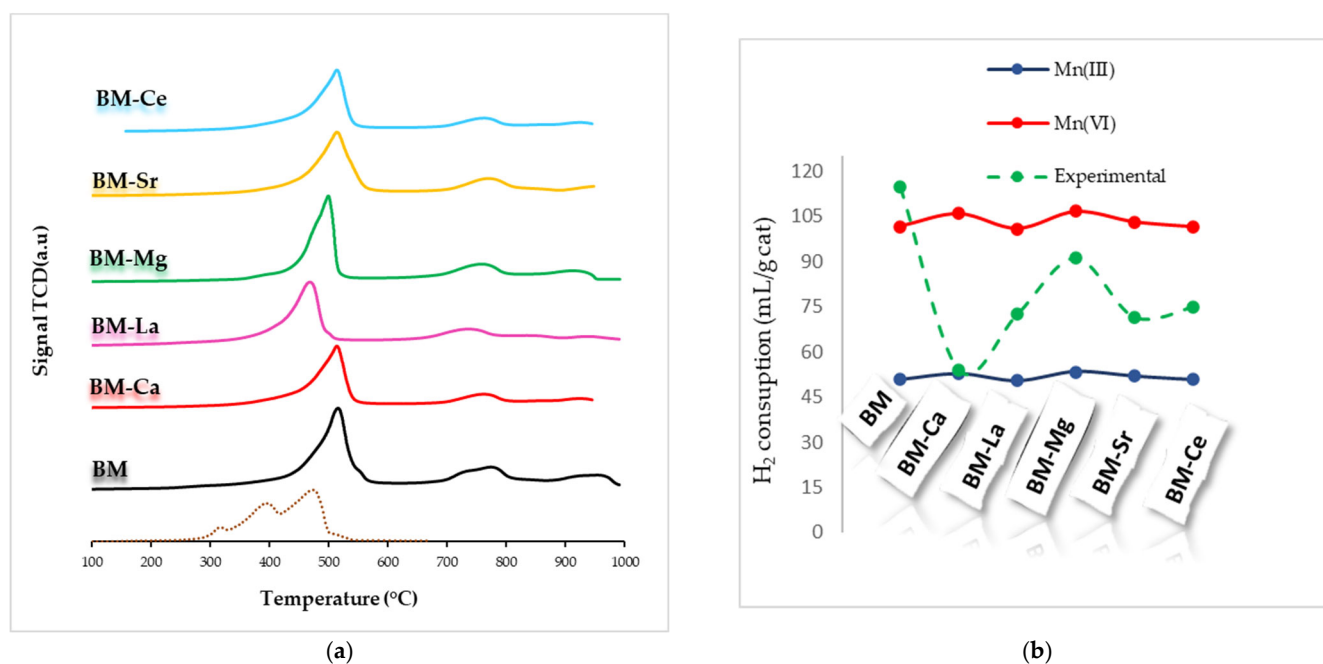


**Figure 3.** H<sub>2</sub>-TPR profiles of BM-A, BM catalysts, and MnO<sub>2</sub>, used as a reference (a) and H<sub>2</sub> consumption (mL/g of catalyst) (b).

O<sub>2</sub>-TPD tests provide information about the labile oxygen species of the catalysts and about their oxygen mobility [10,36,45], as shown in the profiles displayed in Figure 4a. For perovskites, three oxygen desorption regions are usually detected: (i) the peak located between 150 °C and 350 °C, for the oxygen evolving from the adsorbed on the surface vacancies (called  $\alpha$ -O<sub>2</sub>); (ii) the peak appearing between 500 °C and 700 °C, corresponding to the oxygen located on surface lattice defects, such as dislocation or grain frontiers (denoted as  $\alpha'$ -O<sub>2</sub>); and (iii) the peak over 700 °C, generated by the desorption of lattice oxygen (designed as  $\beta$ -O<sub>2</sub>) due to the reduction of manganese in the perovskite lattice and related to the oxygen mobility through the bulk [10,32,42,45]. Thus, BM-Ca, BM-Ce, and BM-Mg samples evolve oxygen above 700 °C, coming from the perovskite lattice ( $\beta$ -oxygen), which depends on the partial reduction of Mn(IV) to Mn(III) [32,42,46,49], and for BM-Ce, also on the Ce(IV)/Ce(III) redox pair [50]. However, BM-La and BM-Sr do not follow the described trend, as BM-La shows a certain oxygen desorption at a temperature below 700 °C, which corresponds to  $\alpha'$ -O<sub>2</sub>, and BM-Sr presents a desorption profile similar to the raw perovskite (BM) without clearly defined peaks. Figure 4b features the amount of  $\beta$ -O<sub>2</sub> evolved, calculated with the area of the peak between 700 °C and 950 °C (except for BM-La) and CuO as a reference for the quantification. It is observed that, due to the partial replacement of Ba with A metals, the amount of O<sub>2</sub> released increases, mainly for BM-Ce due to the contribution of the Ce(IV)/Ce(III) redox pair. This finding reveals an increase in the mobility of  $\beta$ -O<sub>2</sub> due to the presence of A metals, showing BM-Ce the highest value.

### 3.1.2. Ba<sub>0.9</sub>A<sub>0.1</sub>Mn<sub>0.7</sub>Cu<sub>0.3</sub>O<sub>3</sub> Series

The nomenclature of catalysts, the BET surface area, the XRD data, and the A and Cu metal contents (obtained by ICP-OES) are reported in Table 3. The ICP-OES data confirm that almost all samples contain the amount of metals (Cu and A) supplied during the synthesis. Additionally, a low surface area is shown for BMC, and the addition of A metal does not significantly affect this parameter. This observation remains consistent with what was previously mentioned for the BM-A series of catalysts.



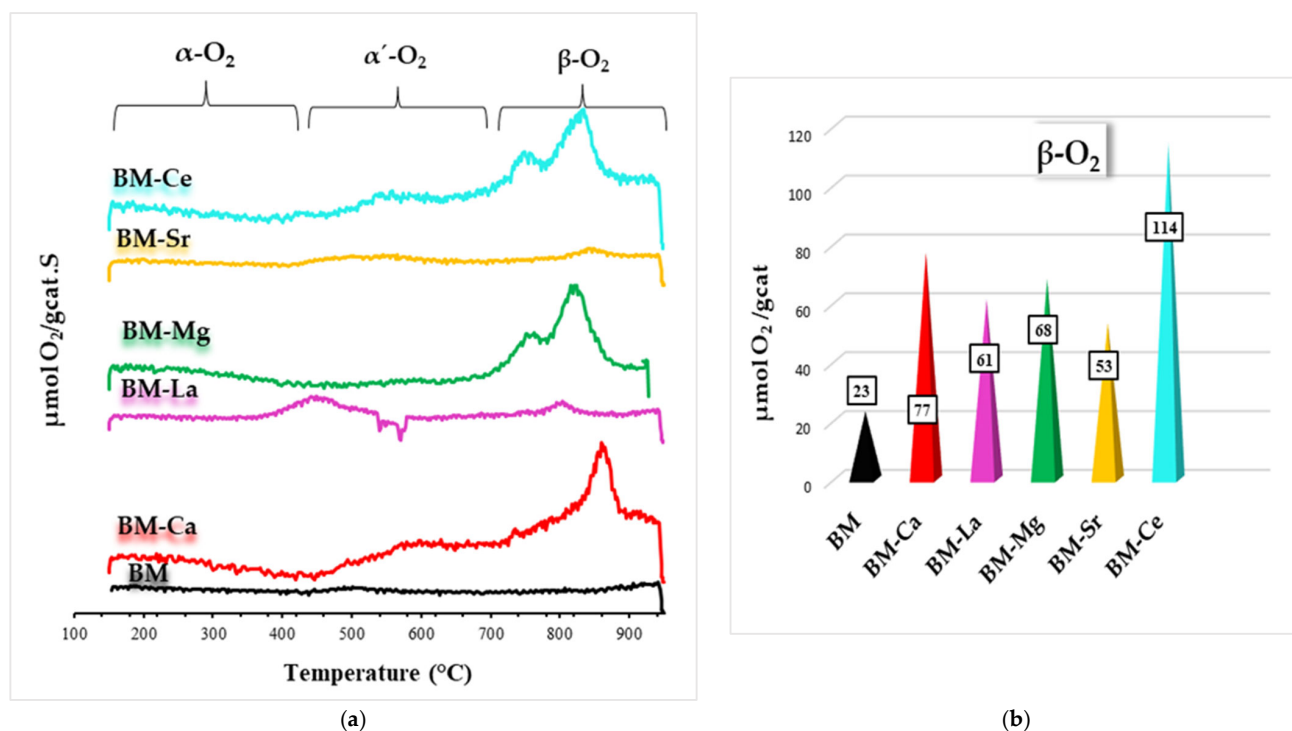


Figure 4. O<sub>2</sub>-TPD profiles (a) and  $\beta$ -O<sub>2</sub> amount ( $\mu\text{mol/g cat}$ ) (b) of BM and BM-A catalysts.

Table 3. Nomenclature, XRD data, A and Cu metal contents, and BET surface area of BMC-A catalysts.

| Nomenclature | Molecular Formula  | A (wt%) | Cu (wt%) | BET (m <sup>2</sup> /g) | 2 $\Theta$ (°) <sup>a</sup> | Intensity (a.u.) <sup>a</sup> | Average Crystal (nm) | Cell Parameters (Å) <sup>b</sup> |          |
|--------------|--|---------|----------|-------------------------|-----------------------------|-------------------------------|----------------------|----------------------------------|----------|
|              |  |         |          |                         |                             |                               |                      | <i>a</i>                         | <i>c</i> |
| BMC          | BaMn <sub>0.7</sub> Cu <sub>0.3</sub> O <sub>3</sub>                                   | -       | 8.0      | 3                       | 30.9                        | 2448                          | 30.7                 | 5.8                              | 4.3      |
| BMC-Ca       | Ba <sub>0.9</sub> Ca <sub>0.1</sub> Mn <sub>0.7</sub> Cu <sub>0.3</sub> O <sub>3</sub> | 2.0     | 9.8      | 7                       | 31.0                        | 1154                          | 29.3                 | 5.7                              | 4.3      |
| BMC-La       | Ba <sub>0.9</sub> La <sub>0.1</sub> Mn <sub>0.7</sub> Cu <sub>0.3</sub> O <sub>3</sub> | 5.4     | 9.8      | 7                       | 30.9                        | 2064                          | 18.6                 | 5.8                              | 4.2      |
| BMC-Mg       | Ba <sub>0.9</sub> Mg <sub>0.1</sub> Mn <sub>0.7</sub> Cu <sub>0.3</sub> O <sub>3</sub> | 1.0     | 9.6      | 3                       | 30.9                        | 1246                          | 25.9                 | 5.8                              | 4.3      |
| BMC-Sr       | Ba <sub>0.9</sub> Sr <sub>0.1</sub> Mn <sub>0.7</sub> Cu <sub>0.3</sub> O <sub>3</sub> | 3.9     | 9.1      | 9                       | 31.1                        | 1913                          | 25.0                 | 5.8                              | 4.3      |
| BMC-Ce       | Ba <sub>0.9</sub> Ce <sub>0.1</sub> Mn <sub>0.7</sub> Cu <sub>0.3</sub> O <sub>3</sub> | 2.1     | 9.2      | 6                       | 30.9                        | 1441                          | 22.4                 | 5.6                              | 4.3      |

<sup>a</sup> Corresponding to the main peak of BaMnO<sub>3</sub> polytype structure, <sup>b</sup> Calculated using the main diffraction peak of BaMnO<sub>3</sub> polytype structure.

Figure 5 features the XRD patterns of all samples. The diffraction peaks for BMC catalyst at 27.0°, 30.9°, 27.5°, 41.5°, 52.9°, 54.8°, 64.3, and 71.0° 2 $\Theta$  values perfectly match with the BaMnO<sub>3</sub> polytype perovskite structure [32,36], which is formed because copper partially replace the manganese in the perovskite lattice and causes a different order of the MO<sub>6</sub> units [51]. However, in BMC-A samples, the polytype structure partially changed back into the hexagonal 2H-BaMnO<sub>3</sub> structure, thus confirming that A metal has been inserted into the lattice of perovskite. For BMC-La, a peak corresponding to BaMn<sub>2</sub>O<sub>3</sub> is also detected as a minority phase. The presence of the hexagonal perovskite structure, in addition to the polytype one, could be related to the presence of A metal, which hinders the introduction of copper into the perovskite network. However, as copper species (as CuO) are not clearly detected by XRD, it seems that copper should be inserted into the BM-A perovskites without causing a significant distortion of the hexagonal structure of BaMnO<sub>3</sub>, so this structure seems to be partially preserved for BMC-A. In fact, the coexistence of both hexagonal and polytype structures was previously observed by the authors for under stoichiometric Ba-Cu-Mn perovskites (Ba<sub>0.9</sub>Cu<sub>0.3</sub>Mn<sub>0.7</sub>O<sub>3</sub> and Ba<sub>0.8</sub>Cu<sub>0.3</sub>Mn<sub>0.7</sub>O<sub>3</sub>) [52]. The transition of the polytype structure to the hexagonal one in BMC-A samples is also evidenced by the decrease in the intensities of the main XRD peak of the former crystalline phase (see values included in Table 3). So, if A metal is present in the catalytic formulation,

the crystal growth of the polytype phase seems to be hindered in favour of the formation of the hexagonal structure.

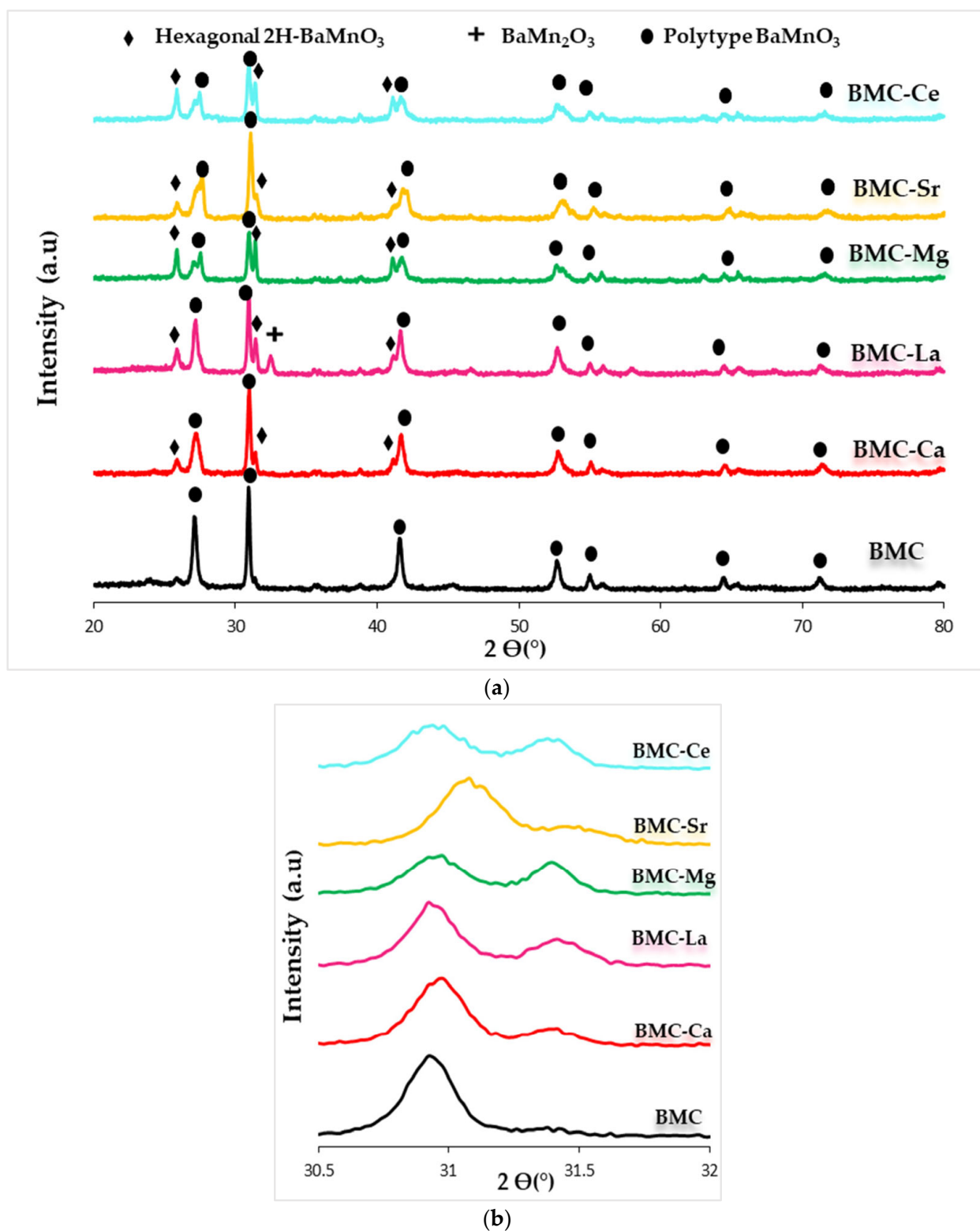


**Figure 5.** (a) XRD profiles of BMC-A and BMC catalysts and (b) magnification of the  $2\theta$  diffraction angle region corresponding to main diffraction peak of hexagonal and polytype structure of  $\text{BaMnO}_3$ .

To deeply analyze the partial replacement of Ba by A metal, in Figure 5b, the  $2\theta$  diffraction angle between  $30.5^{\circ}$  and  $32.5^{\circ}$  (where the main peak of hexagonal and polytype

perovskite structures appear, respectively) has been magnified. A slight displacement of the polytype structure main peak to higher diffraction angles with respect to BMC is observed for BMC-Sr catalyst, being less pronounced for BMC-Ca. In this line, Albaladejo-Fuentes and co-workers [53] reported a structural distortion for the  $\text{Ba}_{0.9}\text{Sr}_{0.1}\text{Ti}_{0.8}\text{Cu}_{0.2}\text{O}_3$  (BTCu-Sr) perovskite due to the partial replacement of Ba(II) by Sr(II). Also, a shift of the main XRD peak was detected by Fu and coworkers [54] due to the presence of the smaller Ca(II) ions in the Ba-site in the  $\text{Ba}_{1-x}\text{Ca}_x\text{TiO}_3$  catalyst series. Concerning BMC-La, BMC-Ce, and BMC-Mg catalysts, as a change in the position of the polytype  $\text{BaMnO}_3$  structure peak is not clearly detected, it looks as if the A position of the perovskite structure does not include cerium, lanthanum, or magnesium. According to the effect of magnesium on the structure of  $\text{BaTiO}_3$  [53,55], in which Mg(II) was located in the Ti(IV) position, in BMC-Mg, Mg(II) could be replacing Cu and/or Mn instead of Ba. Thus, based on the ionic radius values shown in Table 4, it is suggested that Mg could be incorporated in the B-site (partially replacing Cu and/or Mn) since the ionic radius of Mg(II) is closer to Mn(III) and Cu(II) ionic radii than to Ba(II) radius. However, Ce and La cations should be placed in the A site, since their ionic radii are closer to those of Ba(II), but it seems that this fact happens without a significant distortion of the hexagonal structure. As for the BM-A series, the Williamson-Hall method [39] was applied to determine the average crystallite size of the polytype perovskite phase included in Table 3. The average crystallite size of perovskite decreases for BMC-A samples, achieving the lowest value for BMC-La. On the contrary, the *a* and *c* parameters of BMC-A do not change with respect to the BMC, and only the BMC-Ce catalyst displays a small distortion of the polytype structure.

**Table 4.** Ionic radii of cation metals using the Goldshmidt correction [16,31,35].

| Metals           | Ba(II) | Ca(II) | Mg(II) | La(III) | Ce(IV) | Ce(III) | Sr(II) | Cu(II) | Mn(IV) | Mn(III) |
|------------------|--------|--------|--------|---------|--------|---------|--------|--------|--------|---------|
| Ionic radii (pm) | 146.4  | 115.5  | 65.0   | 107.3   | 90.6   | 105.2   | 129.9  | 73.0   | 53.0   | 65.0    |

The XPS spectra for the O 1s, Mn 2p<sub>3/2</sub>, and Cu 2p<sub>3/2</sub> transitions are shown in Figure 6.

The O 1s spectra of BMC and BMC-A (Figure 6a) feature the three contributions previously described for BM and BM-A, and Table 5 displays some relevant XPS data. Focusing attention on the binding energies corresponding to the maximum of the O<sub>L</sub> and O<sub>ads</sub> deconvoluted peaks, BMC-Mg shows the highest chemical shift towards higher binding energies for the O<sub>L</sub> peak, even though it is very low (0.2 eV). It is important to remember that a shift of the deconvoluted band towards lower binding energies indicates the existence of a richer electronic environment, whereas a displacement towards higher binding energies indicates the opposite. So, the displacement of the O<sub>L</sub> peak to higher binding energies reveals a poor electronic environment created because of the loss of oxygen from the MnO<sub>6</sub> octahedra, which, in order to achieve electroneutrality, takes place when Mg(II) occupies the Mn sites. As the O<sub>L</sub>/(Ba + Mn + Cu + A) nominal ratio (1.5) is higher than the XPS one for all perovskites, oxygen surface vacancies exist on all samples. As discussed above for the BM-A series, this fact is caused by the coexistence of surface Mn(III) and Cu(II) [32]. Note that all BMC-A catalysts (except for BMC-Ca) present a slightly higher value of O<sub>L</sub>/(Ba + Mn + Cu + A) ratio than BMC, so it seems that the partial substitution of Ba by A metal in BMC slightly decreases the presence of surface oxygen vacancies.

Figure 6b presents the Mn 2p<sub>3/2</sub> XPS spectra of BMC and BMC-A samples, where Mn(III) and Mn(IV) signals and Mn(III) satellite contributions were indexed, with Mn(IV) located at 642.4 eV, Mn(III) at 641.2 eV, and the Mn(III) satellite at 644.0 eV [56]. Table 5 provides the binding energy corresponding to the maximum of these deconvoluted peaks and, also, the Mn(IV)/Mn(III) ratios. Note that the presence of A metal does not significantly modify the binding energy for Mn(III) and Mn(IV) peaks, being the highest change observed for Mn(III) in BMC-Mg, which, in turn, is low (0.2 eV) and seems to be related to the location of Mg(II) in the Mn site. After doping with A metals, a significant change in the Mn(IV)/Mn(III) ratio is not observed, as the Mn(IV)/Mn(III) ratio decreases from 1.3 to

1.2 for most BMC-A samples, from 1.3 to 1.1 for BMC-La, and is not modified for BMC-Sr. However, as the ratios are higher than 1, Mn(IV) is the main oxidation state on the surface.

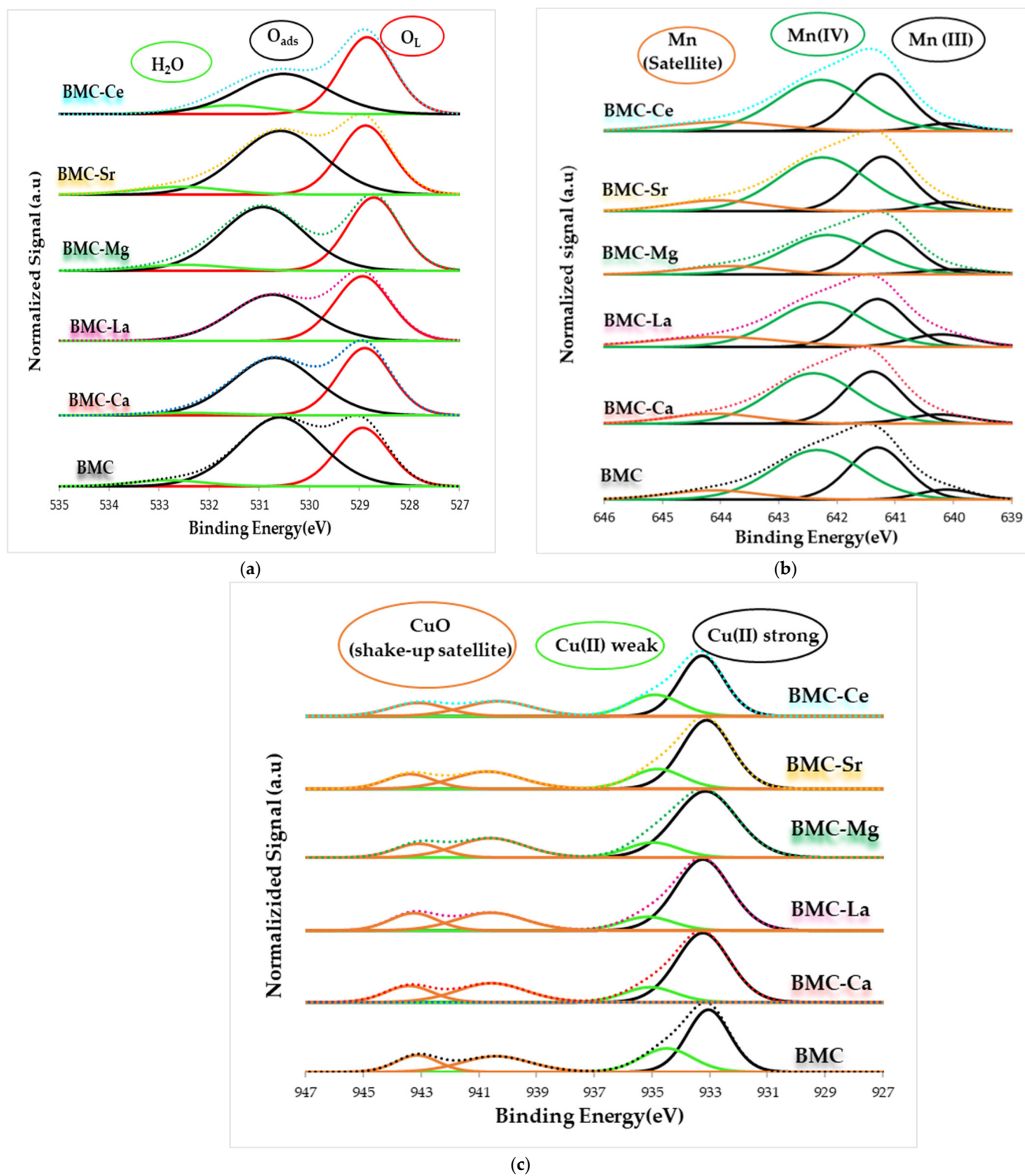


**Figure 6.** XPS spectra of BMC-A and BMC catalysts in the (a) O 1s and (b) Mn  $2p_{3/2}$  and (c) Cu  $2p_{3/2}$  core level regions.

**Table 5.** XPS data of BMC-A and BMC catalysts.

| Catalyst | B.Emax<br>Cu(II) <sub>s</sub> <sup>a</sup><br>(eV) | B.Emax<br>Cu(II) <sub>w</sub> <sup>b</sup><br>(eV) | B.Emax<br>Mn(III)<br>(eV) | B.Emax<br>Mn(IV)<br>(eV) | B.Emax<br>O <sub>L</sub> (eV) | B.Emax<br>O <sub>ads</sub> (eV) | $\frac{\text{Mn(IV)}}{\text{Mn(III)}}$ | $\frac{\text{Cu}}{\text{M}}$ <sup>c</sup><br>(Nominal = 0.15) | $\frac{\text{O}_L}{\text{M}}$ <sup>c</sup><br>(Nominal = 1.5) |
|----------|--|--|---------------------------|--------------------------|-------------------------------|---------------------------------|--|---|---|
| BMC      | 933.1  | 934.5  | 641.3                     | 642.3                    | 528.9                         | 530.6                           | 1.3                                    | 0.09  | 0.8   |
| BMC-Ca   | 933.3  | 934.9  | 641.4                     | 642.4                    | 528.9                         | 530.7                           | 1.2                                    | 0.07  | 0.8   |
| BMC-La   | 933.2  | 935.1  | 641.3                     | 642.3                    | 528.9                         | 530.7                           | 1.1                                    | 0.10  | 0.9   |
| BMC-Mg   | 933.1  | 935.0  | 641.1                     | 642.2                    | 528.7                         | 530.9                           | 1.2                                    | 0.09  | 0.9   |
| BMC-Sr   | 933.2  | 935.2  | 641.2                     | 642.3                    | 528.9                         | 530.6                           | 1.3                                    | 0.09  | 0.9   |
| BMC-Ce   | 933.1  | 934.8  | 641.3                     | 641.3                    | 528.8                         | 530.5                           | 1.2                                    | 0.07  | 0.9   |

<sup>a</sup> s = strong, <sup>b</sup> w = weak, <sup>c</sup> M = Ba + Mn + Cu.

The Cu 2p<sub>3/2</sub> XPS profiles featured in Figure 6c reveal that Cu(II) exists on the surface, as the XPS peaks close to 933.0 eV appear and because the satellite peaks expected for Cu(II) (at 940.0 eV and 943.0 eV) are also present [32]. Additionally, after deconvolution, two contributions are detected at ca. 933.0 eV and 934.5 eV (see Table 5), which can be attributed to Cu(II) with strong (Cu(II)<sub>s</sub>) and weak (Cu(II)<sub>w</sub>) interactions with the perovskites, respectively [23,32,38]. After A doping, an increase in the binding energy corresponding to the maximum of Cu(II)<sub>w</sub> is detected, which indicates the presence of a poorer electronic environment than in raw BMC caused by the insertion of A metal. In Table 5, the Cu/(Ba + Mn + Cu + A) ratios are lower than the nominal ones (0.15), so it seems that Cu(II) has been inserted into the perovskite structure for all samples. Note that, after the addition of Ce or Ca, the ratio decreases to 0.07, and, for La, it increases to 0.1. Thus, the distribution of copper is only modified with respect to BMC for Ce, Ca, and La metals: Ce and Ca seem to promote the introduction of copper into the structure, and La seems to favour a slightly higher proportion of surface copper [23].

H<sub>2</sub>-TPR profiles are shown in Figure 7a, where the corresponding MnO<sub>2</sub> and CuO profiles (divided by 4 to be comparable with the catalyst profiles) have also been included as references. The H<sub>2</sub>-TPR profile for MnO<sub>2</sub>, as above discussed, features two overlapping reduction peaks at around 400 and 500 °C, corresponding to the MnO<sub>2</sub>/Mn<sub>2</sub>O<sub>3</sub> reduction of Mn<sub>3</sub>O<sub>4</sub> and to Mn<sub>3</sub>O<sub>4</sub> to MnO reduction [45]. CuO displayed at ca. 320 °C a single broad reduction peak due to the reduction Cu(II) to Cu(0). The H<sub>2</sub>-TPR profiles of BMC-A samples suggest that the metal reduction occurs in multiple steps:

- Between approximately 200 and 400 °C, the reduction of Mn(IV) and Mn(III) to Mn(II), and also of Cu(II) to Cu(0), takes place.
- Between 700 °C and 800 °C, a small peak attributed to the desorption/reduction of oxygen species is featured.
- Between 900 °C and 1000 °C, a third peak with very low intensity, corresponding to the bulk Mn(III) reduction, seems to be present.

A decrease in the temperature for the reduction of Mn(IV)/Mn(III) to Mn(II) and of Cu(II) to Cu(0) in the H<sub>2</sub>-TPR profiles of BMC-A (Figure 7a) is exclusively detected after Ce doping. In fact, after Mg doping, an increase in temperature is detected, which could be related to the different location of Mg in this sample. The experimental hydrogen consumption per gram of catalyst, determined between 200 °C and 450 °C using the hydrogen consumption profiles shown in Figure 7a, has been compared with the theoretical hydrogen consumption determined considering the total reduction of manganese and copper (as Mn(III) + Cu(II) in the blue line or Mn(IV) + Cu(II) in the red line) in Figure 7b. For BMC-A samples, the experimental H<sub>2</sub> consumptions are between the nominal ones for Mn(IV) + Cu(II) and Mn(III) + Cu(II), corresponding to BMC-Mg and BMC-Ce being closer to Mn(IV) + Cu(II), while for BMC, BMC-Ca, BMC-La, and BMC-Sr are closer to Mn(III) + Cu(II). Thus, it appears that both Mn(III) and Mn(IV) exist in the bulk of perovskites, as detected by XPS on the surface.



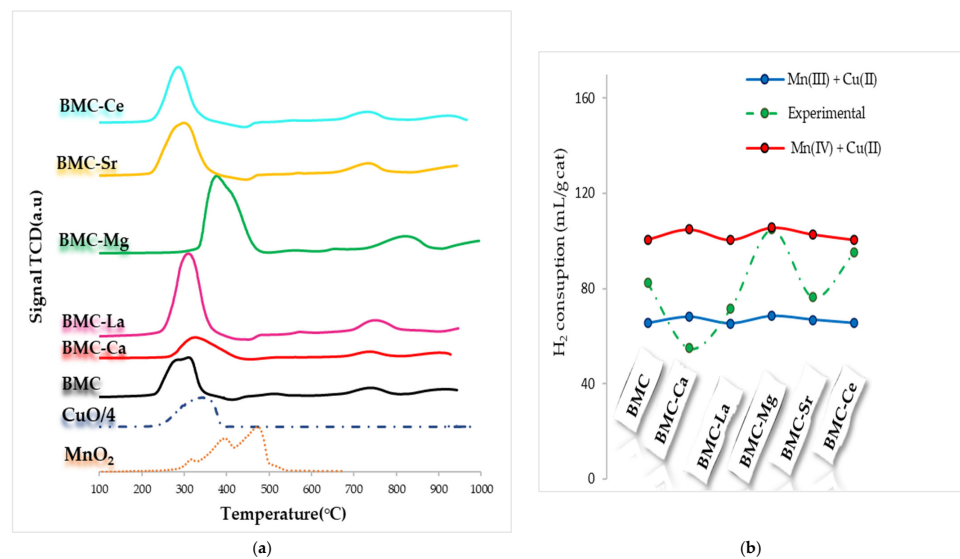


**Figure 7.** H<sub>2</sub>-TPR profiles of BMC-A and BMC catalysts (a) and H<sub>2</sub> consumption (mL/g of catalyst) (b).

O<sub>2</sub>-TPD tests were also performed, and the obtained profiles are illustrated in Figure 8. It is observed that, as previously described for the BM-A series, the catalysts exclusively evolve  $\beta$ -O<sub>2</sub>, which is linked to the reduction of Mn(IV) to Mn(III) and of Cu(II) to Cu(I) [57–61] and, for BMC-Ce, also to the reduction of Ce(IV) to Ce(III) [50]. After A metal is included in the formulation of samples, a shift towards higher temperatures is detected for the temperature of the maximum oxygen emission. This fact is directly related to the A-O bond energy, which is expected to be higher than the Ba-O bond energy, as Ba(II) presents a larger ionic radius than the A metal (see Table 4). As shown in Figure 8b, the partial substitution of Ba causes an increase in the amount of  $\beta$ -O<sub>2</sub> released, which is evidence of the improved mobility of the bulk oxygen, according to the following trend: BMC-Ce > BMC-Ca > BMC-Mg > BMC-Sr > BMC-La > BMC. This finding seems to be related, in general terms, to the reducibility of the samples, as BMC-Ce is the most reducible catalyst and has also evolved the highest amount of oxygen.

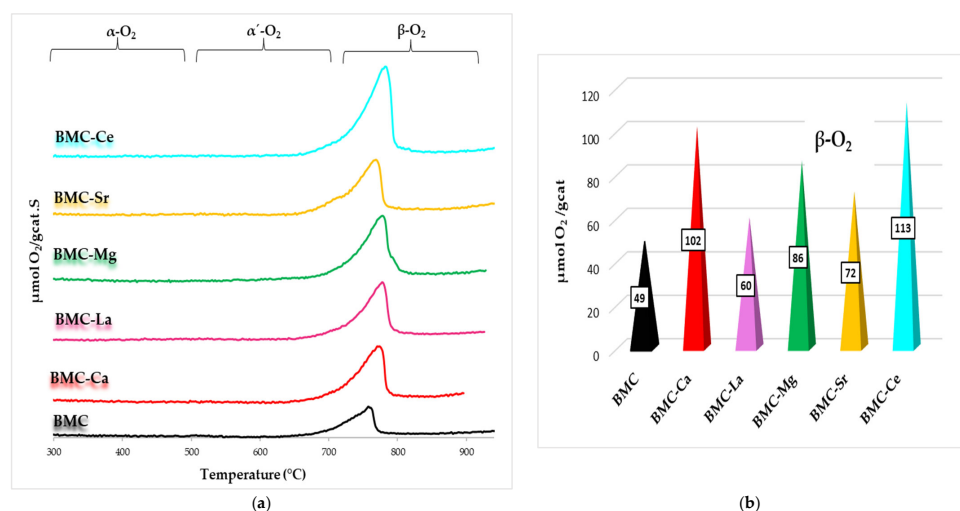


**Figure 8.** O<sub>2</sub>-TPD profiles of BMC and BMC-A catalysts (a) and  $\beta$ -O<sub>2</sub> amount emitted during O<sub>2</sub>-TPD experiments (b).

In summary, by comparing the characterization results for the two series of A-doped catalysts (BM-A and BMC-A), it seems that:

- (i) The hexagonal structure is favoured in the presence of A dopant, as it is the main phase detected for BM-A, and the polytype structure detected in the BMC sample (formed by distortion of the hexagonal perovskite due to copper insertion into the lattice) is not favoured in BMC-A perovskites, presenting a mixture of the two structures. Also, Mn(IV) and Mn(III) coexist on the surfaces of all samples.
- (ii) Oxygen vacancies are present on the surfaces of all perovskites.
- (iii) The partial substitution of Ba in BM and BMC enhances the reducibility and the lattice oxygen mobility, making Ce the most efficient A metal due to the contribution of the Ce(IV)/Ce(III) redox pair.

### 3.2. Catalytic Activity

#### 3.2.1. BM-A Series

To assess the role of perovskites as GPF catalysts to be used for soot removal in simulated GDI engine exhaust conditions, soot-TPR tests in the two gaseous mixtures previously described (0% and 1% O<sub>2</sub> in He) were carried out [23,24,31], being the soot conversion profiles featured in Figure 9. Table 6 contains the T<sub>10%</sub> and T<sub>50%</sub> values, that are the temperatures for the 10% and 50% of soot conversion, respectively, and the selectivity to CO<sub>2</sub> during the reaction.

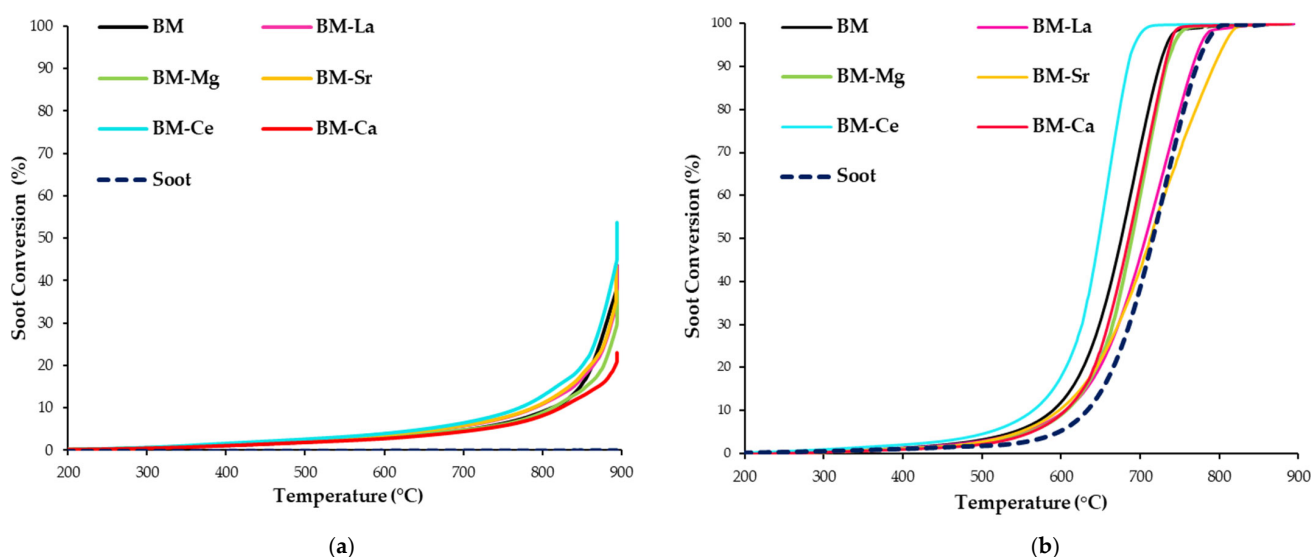


**Figure 9.** Soot-TPR conversion profiles as a function of temperature of BM and BM-A catalysts in 100% He (a) and in 1% O<sub>2</sub>/He (b).

**Table 6.** T<sub>10%</sub>, T<sub>50%</sub>, and selectivity to CO<sub>2</sub> (S<sub>CO2</sub>) for soot oxidation of BM and BM-A catalysts.

| Catalysts | 1% O <sub>2</sub> /He |                       |                       | 100% He               |
|-----------|-----------------------|-----------------------|-----------------------|-----------------------|
|           | S <sub>CO2</sub> (%)  | T <sub>50%</sub> (°C) | T <sub>10%</sub> (°C) | T <sub>10%</sub> (°C) |
| Soot      | 44                    | 714                   | 631                   | -                     |
| BM        | 73                    | 710                   | 610                   | 813                   |
| BM-La     | 93                    | 708                   | 606                   | 791                   |
| BM-Mg     | 92                    | 684                   | 589                   | 813                   |
| BM-Sr     | 93                    | 711                   | 591                   | 789                   |
| BM-Ce     | 90                    | 641                   | 548                   | 772                   |
| BM-Ca     | 91                    | 680                   | 584                   | 823                   |

Note that almost all samples catalyze the soot oxidation reaction, as most of the profiles are shifted to lower temperatures with respect to the uncatalyzed reaction (soot in Figure 9) in the two atmospheres tested. The soot conversion in the 100% He begins to be significant at above 700 °C (Figure 9a), while in the 1% O<sub>2</sub>, the soot conversion starts being relevant at around 450 °C (Figure 9b). So, as previously concluded [23,31], soot oxidation is improved in the presence of oxygen in the gaseous mixture used for the reaction. Thus, in the He atmosphere, soot oxidation does not occur in the absence of a catalyst, as there is no oxygen available. However, in the presence of perovskites, the reaction takes place with the oxygen coming from the bulk of mixed oxides ( $\beta$ -O<sub>2</sub>), whose emission was promoted by the Mn(IV) to Mn(III) reduction [31], as well as by the Ce(IV) to Ce(III) reduction in the case of the BM-Ce catalyst [50]. In the 1% O<sub>2</sub> atmosphere, BM-Ca, BM-Ce, and BM-Mg show a higher soot conversion than BM, giving BM-Ce the best catalytic performance.

Thus, the data in Table 6 reveal that the partial replacement of Ba by A metal in BM perovskite improves the catalytic performance for soot removal in simulated GDI engine conditions, as T<sub>10%</sub> and T<sub>50%</sub> values decrease with respect to BM for most A metals. BM-Ce is the best catalyst in the two conditions tested, as it presents the lowest T<sub>10%</sub> and T<sub>50%</sub> values. This sample presents the highest oxygen mobility due to the contribution of Ce(IV)/Ce(III) along with the Mn(IV)/Mn(III), which enhances the redox reaction and the oxygen emission, which is directly involved in the soot oxidation. Additionally, oxygen vacancies exist on the surface (as O<sub>L</sub>/(Ba + Mn + Cu) XPS ratios are lower than 1.5) that work as active sites where the oxygen from the gas phase is activated and participates in the soot oxidation reaction. So, the more efficient activation of oxygen on the active sites and the higher release of oxygen from the catalyst make BM-Ce the most active sample of the BM-A series.

Finally, regarding CO<sub>2</sub> selectivity, all BM-A catalysts improve this parameter with respect to BM, so these catalysts seem to be also promising for CO oxidation reactions.

### 3.2.2. BMC-A Series

In order to determine the impact of A metal doping (A = La, Mg, Sr, Ce, Ca) on the catalytic performance of BMC samples for soot removal, as for the BM-A series, soot-TPR tests have been developed using conditions similar to those of GDI engine exhaust. The soot conversion profiles are displayed in Figure 10a,b, and Table 7 summarizes the temperatures needed to achieve 10% and 50% soot conversion, respectively, as well as the selectivity to CO<sub>2</sub>.

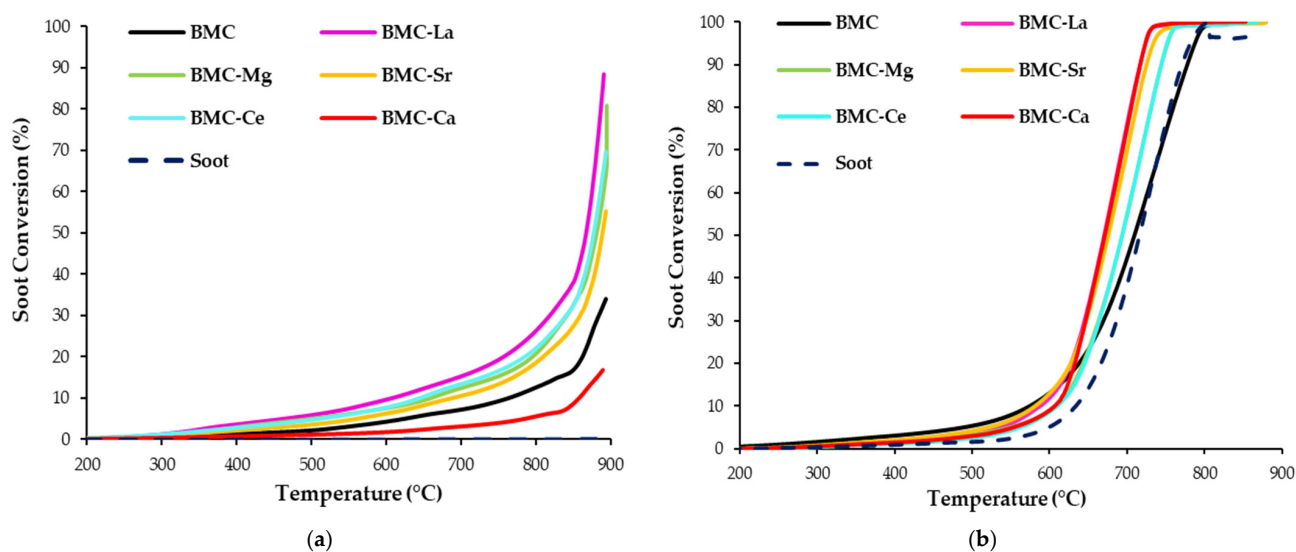


**Figure 10.** Soot conversion profiles as a function of temperature of BMC and BMC-A catalysts in: (a) 100% He and (b) 1% O<sub>2</sub>/He.

**Table 7.**  $T_{10\%}$ ,  $T_{50\%}$  and selectivity to  $\text{CO}_2$  ( $S_{\text{CO}_2}$ ) for soot oxidation in the two tested atmospheres of BMC and BMC-A catalysts.

| Catalysts | 1% $\text{O}_2/\text{He}$ |                    |                    | 100% He            |                          |
|-----------|---------------------------|--------------------|--------------------|--------------------|--------------------------|
|           | $S_{\text{CO}_2}$<br>(%)  | $T_{50\%}$<br>(°C) | $T_{10\%}$<br>(°C) | $T_{10\%}$<br>(°C) | $S_{\text{CO}_2}$<br>(%) |
| Soot      | 44                        | 756                | 631                | -                  | -                        |
| BMC       | 70                        | 732                | 599                | 879                | 33                       |
| BMC-Ca    | 93                        | 671                | 606                | 859                | 37                       |
| BMC-La    | 94                        | 671                | 588                | 611                | 40                       |
| BMC-Mg    | 92                        | 695                | 605                | 660                | 25                       |
| BMC-Sr    | 88                        | 712                | 582                | 689                | 27                       |
| BMC-Ce    | 94                        | 693                | 610                | 646                | 32                       |

First, focusing on the results obtained using 100% He (Figure 10a), all perovskites are active for soot oxidation since the uncatalyzed reaction (denoted as soot in Figure 10) does not take place as there is no oxygen available for the reaction. Note that, after doping BMC with A metal, all the soot conversion profiles are shifted to lower temperatures with respect to BMC. However, the catalytic activity is notably lower than in the 1%  $\text{O}_2$  atmosphere, as the oxygen involved in soot oxidation only comes from the bulk of samples. The BMC-La sample exhibits the lowest  $T_{10\%}$ , probably due to the highest amount of copper on the surface (see Table 5), which is active for soot oxidation [33]. According to the literature, this surface copper species are present as  $\text{BaO}_x\text{-CuO}_x$  phases, forming Cu–O–Ba units in the interface between CuO and the perovskite [24]. As the Cu–O bond energy is lower than that of the Mn–O bond, the release of oxygen from Cu–O–Ba units is easier, thus allowing a high oxygen release rate that improves the catalytic performance for soot oxidation [62]. Aneggi et al. [5], using ceria-zirconia Cu-based catalysts, also detected an improvement in the catalytic activity for soot removal in the absence of oxygen due to the well-known high Oxygen Storage Capacity (OSC) of these mixed oxides. In the 1%  $\text{O}_2/\text{He}$  reactant mixture, the addition of A metal also enhances the catalytic activity for soot oxidation, and  $T_{50\%}$  values for BMC-A samples are lower than those corresponding to the raw BMC. In these conditions, BMC-Ca and BMC-La are the most active formulations, as these catalysts increase the amount of oxygen evolved (according to  $\text{O}_2$ -TPD results) and present more oxygen vacancies (that allow the activation of oxygen from the gas phase) and surface copper species with a poorer electronic environment than raw BMC (see XPS results); this gives BMC-La the highest proportion of surface copper. In this sense, W.Y. Hernández et al. [63] also found that the use of  $\text{La}_{0.6}\text{Sr}_{0.4}\text{FeO}_3$  and  $\text{La}_{0.6}\text{Sr}_{0.4}\text{MnO}_3$  allows a notable decrease in the light-off temperatures in the 1%  $\text{O}_2/\text{He}$  atmosphere. On the other hand, according to other papers [24,46], the  $\text{CO}_2$  selectivity values are higher when oxygen is present in the reaction atmosphere, and the generation of  $\text{CO}_2$  is highly favoured by A doping, being around 90% for all samples. Thus, as well as the BM-A series, these samples are promising catalysts for the CO oxidation reaction.

Finally, by comparing the  $T_{10\%}$  and  $T_{50\%}$  values of the best catalysts of the two series analyzed (BM-Ce and BMC-La, selected because they featured the highest selectivity to  $\text{CO}_2$ ), it could be concluded that:

- (i) In 100% He, BMC-La is the most active catalyst, as  $T_{10\%}$  is lower than the observed for BMC-Ce (611 °C and 646 °C, respectively), mainly because more copper (as BaO–CuO species) is present on the surface of BMC-La than on BMC-Ce (Cu/(Ba + Mn + Cu + A) ratios are 0.10 and 0.07, respectively).
- (ii) In 1%  $\text{O}_2$  in He, the best catalyst is BM-Ce, as it presents a lower  $T_{50\%}$  value than BMC-La (641 °C and 671 °C, respectively) and a similar  $\text{CO}_2$  selectivity (around 90% in both catalysts). BM-Ce is the sample with the highest oxygen mobility and the best

redox properties due to the participation of the Ce(IV)/Ce(III) redox pair as well as a high amount of oxygen vacancies on the surface.

So, according to the previous discussion, the role of copper seems to be relevant if the oxygen involved in the soot oxidation comes from the perovskite (i.e., in 100% He), and BMC-La is the most active catalyst as it presents the highest fraction of copper on the surface. However, if soot is oxidized using the oxygen present in the reaction atmosphere (i.e., in 1% O<sub>2</sub> in He), the presence of copper in the perovskite composition seems not to be significant, as the most active catalyst is BM-Ce. Note that the BM-Ce sample presents a higher fraction of surface Ce(IV) than BMC-Ce (see data in Appendix A), so it has better redox performance.

#### 4. Conclusions

In this paper, Ba<sub>0.9</sub>A<sub>0.1</sub>MnO<sub>3</sub> (BM-A, A = Mg, Ca, Sr, Ce, La) and Ba<sub>0.9</sub>A<sub>0.1</sub>Mn<sub>0.7</sub>Cu<sub>0.3</sub>O<sub>3</sub> (BMC-A, A = Mg, Ca, Sr, Ce, La) perovskite-type mixed oxides were prepared, characterized, and used for soot removal by oxidation in simulated GDI engine exhaust conditions. Considering the results discussed above, the following conclusions can be drawn:

- The hexagonal structure is favoured in the presence of A metal, as it is the main phase detected for BM-A, and the polytype structure found in the BMC sample (formed by distortion of the hexagonal perovskite due to copper insertion into the lattice) is not favoured in BMC-A perovskites that present a mixture of the two structures.
- On the surface of all perovskites, coexisting Mn(IV) and Mn(III) and oxygen vacancies are present.
- The partial substitution of Ba in BM and BMC enhances the reducibility and the lattice oxygen mobility, and Ce is the most efficient due to the contribution of the Ce(IV)/Ce(III) redox pair.
- Almost all samples are active as catalysts for soot removal by oxidation, as most of the conversion profiles are shifted to lower temperatures in the presence of perovskites in the two atmospheres tested (0% and 1% O<sub>2</sub> in He).
- The soot conversion is notably lower in the absence of O<sub>2</sub> than in the 1% O<sub>2</sub> atmosphere, as the oxygen available for soot oxidation exclusively comes from the bulk of samples. In these conditions, BMC-La is the most active catalyst due to its highest proportion of copper on the surface (as Ba-O-Cu species).
- In 1% O<sub>2</sub> in He, BM-Ce is the best catalyst as it presents a high amount of oxygen surface vacancies, the highest oxygen mobility, and the best redox properties due to the participation of the Ce(IV)/Ce(III) pair along with the Mn(IV)/Mn(III) pair that promote the O<sub>2</sub> emission from perovskite, which is directly involved in the soot oxidation.
- The role of copper seems to be relevant only if the oxygen used for the soot oxidation exclusively comes from the perovskite (i.e., in 100% He), as BMC-La, which presents the highest fraction of surface copper, is the most active catalyst. On the contrary, if soot is oxidized using the oxygen present in the reaction atmosphere (i.e., in 1% O<sub>2</sub> in He), the presence of copper in the perovskite composition is not significant, as the most active catalyst is BM-Ce because it presents a higher fraction of surface Ce(IV) than BMC-Ce and, consequently, a better redox performance.

**Author Contributions:** The individual contributions of each author are indicated as follows: N.G.: investigation, resources, data curation, and writing—original draft preparation; Á.D.V.: investigation and resources; M.J.I.G.: conceptualization, methodology, writing—review and editing, visualization, supervision, project administration, and funding acquisition. All authors have read and agreed to the published version of the manuscript.



**Funding:** This research was funded by the Spanish Government (MINCINN: PID2019-105542RB-I00/AEI/10.13039/501100011033 Project), the European Union (FEDER Funds), and Generalitat Valenciana (CIPROM/2021-070 Project). N. Ghezali thanks Argelian Government for her thesis grant and Á. Díaz-Verde of the University of Alicante for his predoctoral contract.

**Conflicts of Interest:** The authors declare no conflict of interest.

## Abbreviations

|                     |  |
|---------------------|--|
| GDI                 | Gasoline direct injection                                    |
| PM                  | Particulate matter   |
| PM2.5               | Particulate matter with a diameter of 2.5 $\mu\text{m}$      |
| GPF                 | Gasoline particulate filter                                  |
| TWC                 | Three-way catalyst   |
| CO <sub>2</sub> RR  | CO <sub>2</sub> reduction reaction                           |
| ORR                 | Oxygen reduction reaction                                    |
| OER                 | Oxygen evolution reaction                                    |
| ICP-OES             | Inductively coupled plasma optical emission spectroscopy     |
| XRD                 | X-ray diffraction  |
| XPS                 | X-ray photoelectron spectroscopy                             |
| H <sub>2</sub> -TPR | Temperature-programmed reduction with H <sub>2</sub>         |
| O <sub>2</sub> -TPD | Temperature-programmed desorption of oxygen                  |
| TCD                 | Thermal conductivity detector                                |
| BE                  | Binding energy   |
| KE                  | Kinetic energy   |
| TG-MS               | Thermal gravimetric mass spectrometry                        |
| Soot-TPR            | Soot oxidation in temperature-programmed reaction conditions |
| BET                 | Brunauer-emmett-teller                                       |
| ICDD                | International centre of diffraction data                     |
| O <sub>L</sub>      | Lattice oxygen   |
| O <sub>ads</sub>    | Adsorbed oxygen species                                      |
| OSC                 | Oxygen storage capacity                                      |
| SCO <sub>2</sub>    | Selectivity to CO <sub>2</sub>                               |

## Appendix A

The deconvoluted Ce 3d spectra and the corresponding XPS data for BM-Ce and BMC-Ce catalysts are shown in Figure A1 and Table A1, respectively. The deconvoluted spectra presents eight sub-peaks: the v quadruplets in the Ce 3d<sub>5/2</sub> area and the u quadruplets in the Ce 3d<sub>3/2</sub> region. The distinctive identifiers for the Ce(III) oxidation state are two subpeaks, v<sub>1</sub> and u<sub>1</sub> (indicated by regions with deeper colours in Figure A1), whereas the other subpeaks are attributed to the Ce(IV) oxidation state [64,65]. The surface Ce(IV) amount in the BM-Ce sample is comparable to that of the CeO<sub>2</sub> sample used as a reference, while the BMC-Ce sample exhibits a larger abundance of Ce(III). This implies that the presence of Ce(III) species seems to be favoured for the copper-containing sample.

$$\text{Ce(III)} = u_1 + v_1 \quad (\text{A1})$$

$$\text{Ce(IV)} = u_0 + u_2 + u_3 + v_0 + v_2 + v_3 \quad (\text{A2})$$

**Table A1.** XPS data of CeO<sub>2</sub>, BM-Ce, and BMC-Ce catalysts.

| Catalyst                               | CeO <sub>2</sub> | BM-Ce | BMC-Ce |
|--|------------------|-------|--------|
| $\frac{\text{Ce(III)}}{\text{Ce(IV)}}$ | 0.54             | 0.93  | 1.33   |

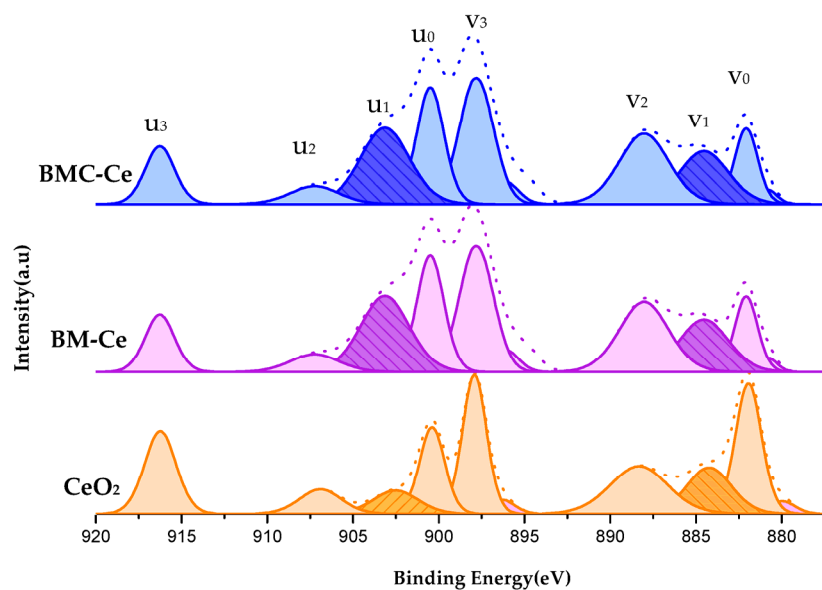


**Figure A1.** Deconvoluted X-ray photoelectron spectra of Ce 3d core levels for BMC-Ce (blue colour), BM-Ce (purple colour) and CeO<sub>2</sub> (orange colour).

## References

- Hamanaka, R.B.; Mutlu, G.M. Particulate Matter Air Pollution: Effects on the Cardiovascular System. *Front. Endocrinol.* **2018**, *9*, 680. [[CrossRef](#)] [[PubMed](#)]
- Xing, J.; Shao, L.; Zhang, W.; Peng, J.; Wang, W.; Hou, C.; Shuai, S.; Hu, M.; Zhang, D. Morphology and Composition of Particles Emitted from a Port Fuel Injection Gasoline Vehicle under Real-World Driving Test Cycles. *J. Environ. Sci.* **2019**, *76*, 339–348. [[CrossRef](#)]
- Wang, J.; Zhao, B.; Wang, S.; Yang, F.; Xing, J.; Morawska, L.; Ding, A.; Kulmala, M.; Kerminen, V.-M.; Kujansuu, J.; et al. Particulate Matter Pollution over China and the Effects of Control Policies. *Sci. Total Environ.* **2017**, *584–585*, 426–447. [[CrossRef](#)]
- Liu, H.; Li, Z.; Zhang, M.; Xu, H.; Ma, X.; Shuai, S. Exhaust Non-Volatile Particle Filtration Characteristics of Three-Way Catalyst and Influencing Factors in a Gasoline Direct Injection Engine Compared to Gasoline Particulate Filter. *Fuel* **2021**, *290*, 120065. [[CrossRef](#)]
- Aneggi, E.; Trovarelli, A. Potential of Ceria-Zirconia-Based Materials in Carbon Soot Oxidation for Gasoline Particulate Filters. *Catalysts* **2020**, *10*, 768. [[CrossRef](#)]
- Varga, T.; Ballai, G.; Vászárhelyi, L.; Haspel, H.; Kukovecz, Á.; Kónya, Z. Co<sub>4</sub>N/Nitrogen-Doped Graphene: A Non-Noble Metal Oxygen Reduction Electrocatalyst for Alkaline Fuel Cells. *Appl. Catal. B Environ.* **2018**, *237*, 826–834. [[CrossRef](#)]
- Asset, T.; Atanassov, P. Iron-Nitrogen-Carbon Catalysts for Proton Exchange Membrane Fuel Cells. *Joule* **2020**, *4*, 33–44. [[CrossRef](#)]
- Srinivasu, K.; Ghosh, S.K. Transition Metal Decorated Graphyne: An Efficient Catalyst for Oxygen Reduction Reaction. *J. Phys. Chem. C* **2013**, *117*, 26021–26028. [[CrossRef](#)]
- Matarrese, R. Catalytic Materials for Gasoline Particulate Filters Soot Oxidation. *Catalysts* **2021**, *11*, 890. [[CrossRef](#)]
- Peña, M.A.; Fierro, J.L.G. Chemical Structures and Performance of Perovskite Oxides. *Chem. Rev.* **2001**, *101*, 1981–2018. [[CrossRef](#)]
- Yamazoe, N.; Teraoka, Y. Oxidation Catalysis of Perovskites—Relationships to Bulk Structure and Composition (Valency, Defect, Etc.). *Catal. Today* **1990**, *8*, 175–199. [[CrossRef](#)]
- Qi, G.; Li, W. Pt-Free, LaMnO<sub>3</sub> Based Lean NO<sub>x</sub> Trap Catalysts. *Catal. Today* **2012**, *184*, 72–77. [[CrossRef](#)]
- Royer, S.; Duprez, D.; Can, F.; Courtois, X.; Batiot-Dupeyrat, C.; Laassiri, S.; Alamdari, H. Perovskites as Substitutes of Noble Metals for Heterogeneous Catalysis: Dream or Reality. *Chem. Rev.* **2014**, *114*, 10292–10368. [[CrossRef](#)] [[PubMed](#)]
- Xu, J.; Liu, J.; Zhao, Z.; Zheng, J.; Zhang, G.; Duan, A.; Jiang, G. Three-Dimensionally Ordered Macroporous LaCo<sub>x</sub>Fe<sub>1-x</sub>O<sub>3</sub> Perovskite-Type Complex Oxide Catalysts for Diesel Soot Combustion. *Catal. Today* **2010**, *153*, 136–142. [[CrossRef](#)]
- Uppara, H.P.; Dasari, H.; Singh, S.K.; Labhsetwar, N.K.; Murari, M.S. Effect of Copper Doping Over GdFeO<sub>3</sub> Perovskite on Soot Oxidation Activity. *Catal. Lett.* **2019**, *149*, 3097–3110. [[CrossRef](#)]
- Koolen, C.D.; Luo, W.; Züttel, A. From Single Crystal to Single Atom Catalysts: Structural Factors Influencing the Performance of Metal Catalysts for CO<sub>2</sub> Electroreduction. *ACS Catal.* **2023**, *13*, 948–973. [[CrossRef](#)]
- Jiang, J.; Huang, B.; Daiyan, R.; Subhash, B.; Tsounis, C.; Ma, Z.; Han, C.; Zhao, Y.; Effendi, L.H.; Gallington, L.C.; et al. Defective Sn-Zn Perovskites through Bio-Directed Routes for Modulating CO<sub>2</sub>RR. *Nano Energy* **2022**, *101*, 107593. [[CrossRef](#)]
- Zhang, J.; Pham, T.H.M.; Ko, Y.; Li, M.; Yang, S.; Koolen, C.D.; Zhong, L.; Luo, W.; Züttel, A. Tandem Effect of Ag@C@Cu Catalysts Enhances Ethanol Selectivity for Electrochemical CO<sub>2</sub> Reduction in Flow Reactors. *Cell Rep. Phys. Sci.* **2022**, *3*, 100949. [[CrossRef](#)]
- Yadav, P.; Yadav, S.; Atri, S.; Tomar, R. A Brief Review on Key Role of Perovskite Oxides as Catalyst. *ChemistrySelect* **2021**, *6*, 12947–12959. [[CrossRef](#)]

20. Pan, Y.; Xu, X.; Zhong, Y.; Ge, L.; Chen, Y.; Veder, J.-P.M.; Guan, D.; O'Hayre, R.; Li, M.; Wang, G.; et al. Direct Evidence of Boosted Oxygen Evolution over Perovskite by Enhanced Lattice Oxygen Participation. *Nat. Commun.* **2020**, *11*, 2002. [[CrossRef](#)]
21. Zhang, Y.; Chang, T.-R.; Zhou, B.; Cui, Y.-T.; Yan, H.; Liu, Z.; Schmitt, F.; Lee, J.; Moore, R.; Chen, Y.; et al. Direct Observation of the Transition from Indirect to Direct Bandgap in Atomically Thin Epitaxial MoSe<sub>2</sub>. *Nat. Nanotechnol.* **2014**, *9*, 111–115. [[CrossRef](#)]
22. Laursen, A.B.; Kegnæs, S.; Dahl, S.; Chorkendorff, I. Molybdenum Sulfides—Efficient and Viable Materials for Electro—And Photoelectrocatalytic Hydrogen Evolution. *Energy Environ. Sci.* **2012**, *5*, 5577–5591. [[CrossRef](#)]
23. Torregrosa-Rivero, V.; Moreno-Marcos, C.; Albaladejo-Fuentes, V.; Sánchez-Adsuar, M.-S.; Illán-Gómez, M.-J. BaFe<sub>1-x</sub>Cu<sub>x</sub>O<sub>3</sub> Perovskites as Active Phase for Diesel (DPF) and Gasoline Particle Filters (GPF). *Nanomaterials* **2019**, *9*, 1551. [[CrossRef](#)] [[PubMed](#)]
24. Moreno-Marcos, C.; Torregrosa-Rivero, V.; Albaladejo-Fuentes, V.; Sánchez-Adsuar, M.S.; Illán-Gómez, M.J. BaFe<sub>1-x</sub>Cu<sub>x</sub>O<sub>3</sub> Perovskites as Soot Oxidation Catalysts for Gasoline Particulate Filters (GPF): A Preliminary Study. *Top. Catal.* **2019**, *62*, 413–418. [[CrossRef](#)]
25. Cimino, S.; Lisi, L.; De Rossi, S.; Faticanti, M.; Porta, P. Methane combustion and CO oxidation on LaAl<sub>1-x</sub>Mn<sub>x</sub>O<sub>3</sub> perovskite-type oxide solid solutions. *Appl. Catal. B Environ.* **2003**, *43*, 397–406. [[CrossRef](#)]
26. Teraoka, Y.; Nii, H.; Kagawa, S.; Jansson, K.; Nygren, M. Influence of the simultaneous substitution of Cu and Ru in the perovskite-type (La,Sr)MO<sub>3</sub> (M = Al, Mn, Fe, Co) on the catalytic activity for CO oxidation and CO-NO reactions. *Appl. Catal. A Gen.* **2000**, *194–195*, 35–41. [[CrossRef](#)]
27. Petrolekas, P.D.; Metcalfe, I.S. Solid Electrolyte Potentiometric Study of La(Sr)MnO<sub>3</sub> Catalyst During Carbon-Monoxide Oxidation. *J. Catal.* **1995**, *152*, 147–163. [[CrossRef](#)]
28. Roy, C.; Budhani, R.C. Raman, Infrared and x-Ray Diffraction Study of Phase Stability in La<sub>1-x</sub>Ba<sub>x</sub>MnO<sub>3</sub> Doped Manganites. *J. Appl. Phys.* **1999**, *85*, 3124–3131. [[CrossRef](#)]
29. Caignaert, V.; Hervieu, M.; Domengès, B.; Nguyen, N.; Pannetier, J.; Raveau, B. BaMn<sub>1-x</sub>Fe<sub>x</sub>O<sub>3-δ</sub>, an Oxygen-Deficient 6H<sup>+</sup> Oxide: Electron Microscopy, Powder Neutron Diffraction, and Mössbauer Study. *J. Solid State Chem.* **1988**, *73*, 107–117. [[CrossRef](#)]
30. Patcas, F.; Buciuman, F.C.; Zsako, J. Oxygen Non-Stoichiometry and Reducibility of B-Site Substituted Lanthanum Manganites. *Thermochim. Acta* **2000**, *360*, 71–76. [[CrossRef](#)]
31. Torregrosa-Rivero, V.; Sánchez-Adsuar, M.-S.; Illán-Gómez, M.-J. Modified BaMnO<sub>3</sub>-Based Catalysts for Gasoline Particle Filters (GPF): A Preliminary Study. *Catalysts* **2022**, *12*, 1325. [[CrossRef](#)]
32. Torregrosa-Rivero, V.; Albaladejo-Fuentes, V.; Sánchez-Adsuar, M.-S.; Illán-Gómez, M.-J. Copper Doped BaMnO<sub>3</sub> Perovskite Catalysts for NO Oxidation and NO<sub>2</sub>-Assisted Diesel Soot Removal. *RSC Adv.* **2017**, *7*, 35228–35238. [[CrossRef](#)]
33. Albaladejo-Fuentes, V.; López-Suárez, F.E.; Sánchez-Adsuar, M.S.; Illán-Gómez, M.J. Tailoring the Properties of BaTi<sub>0.8</sub>Cu<sub>0.2</sub>O<sub>3</sub> Catalyst Selecting the Synthesis Method. *Appl. Catal. A Gen.* **2016**, *519*, 7–15. [[CrossRef](#)]
34. Özkan, D.Ç.; Türk, A.; Celik, E. Synthesis and characterizations of LaMnO<sub>3</sub> perovskite powders using sol-gel method. *J. Mater. Sci.* **2021**, *32*, 1554–15562. [[CrossRef](#)]
35. Akinlolu, K.; Omolara, B.; Shailendra, T.; Abimbola, A.; Kehinde, O. Synthesis, Characterization and Catalytic Activity of Partially Substituted La<sub>1-x</sub>Ba<sub>x</sub>CoO<sub>3</sub> (x ≥ 0.1 ≤ 0.4) Nano Catalysts for Potential Soot Oxidation in Diesel Particulate Filters in Diesel Engines. *Int. Rev. Appl. Sci. Eng.* **2020**, *11*, 52–57. [[CrossRef](#)]
36. Torregrosa-Rivero, V.; Sánchez-Adsuar, M.-S.; Illán-Gómez, M.-J. Improving the Performance of BaMnO<sub>3</sub> Perovskite as Soot Oxidation Catalyst Using Carbon Black during Sol-Gel Synthesis. *Nanomaterials* **2022**, *12*, 219. [[CrossRef](#)]
37. Jacobsen, C.J.H.; Dahl, S.; Hansen, P.L.; Törnqvist, E.; Jensen, L.; Topsoe, H.; Prip, D.V.; Moenshaug, P.B.; Chorkendorff, I. Structure sensitivity of supported ruthenium catalysts for ammonia synthesis. *J. Mol. Catal. A Chem.* **2000**, *163*, 19–26. [[CrossRef](#)]
38. Diaz-Verde, A.; Torregrosa-Rivero, V.; Illán-Gómez, M.J. Copper Catalysts Supported on Barium Deficient Perovskites for CO Oxidation Reaction. *Top. Catal.* **2023**, *66*, 895–907. [[CrossRef](#)]
39. Aarif Ul Islam, S.; Ikram, M. Structural Stability Improvement, Williamson Hall Analysis and Band-Gap Tailoring through A-Site Sr Doping in Rare Earth Based Double Perovskite La<sub>2</sub>NiMnO<sub>6</sub>. *Rare Met.* **2019**, *38*, 805–813. [[CrossRef](#)]
40. Merino, N.A.; Barbero, B.P.; Eloy, P.; Cadús, L.E. La<sub>1-x</sub>Ca<sub>x</sub>CoO<sub>3</sub> Perovskite-Type Oxides: Identification of the Surface Oxygen Species by XPS. *Appl. Surf. Sci.* **2006**, *253*, 1489–1493. [[CrossRef](#)]
41. Tejuca, L.G.; Fierro, J.L.G. XPS and TPD Probe Techniques for the Study of LaNiO<sub>3</sub> Perovskite Oxide. *Thermochim. Acta* **1989**, *147*, 361–375. [[CrossRef](#)]
42. Khaskheli, A.A.; Xu, L.; Liu, D. Manganese Oxide-Based Catalysts for Soot Oxidation: A Review on the Recent Advances and Future Directions. *Energy Fuel.* **2022**, *36*, 7362–7381. [[CrossRef](#)]
43. Yoon, J.S.; Lim, Y.-S.; Choi, B.H.; Hwang, H.J. Catalytic Activity of Perovskite-Type Doped La<sub>0.08</sub>Sr<sub>0.92</sub>Ti<sub>1-x</sub>M<sub>x</sub>O<sub>3-δ</sub> (M = Mn, Fe, and Co) Oxides for Methane Oxidation. *Int. J. Hydrogen Energy* **2014**, *39*, 7955–7962. [[CrossRef](#)]
44. Shen, M.; Zhao, Z.; Chen, J.; Su, Y.; Wang, J.; Wang, X. Effects of Calcium Substitute in LaMnO<sub>3</sub> Perovskites for NO Catalytic Oxidation. *J. Rare Earths* **2013**, *31*, 119–123. [[CrossRef](#)]
45. Zhang, C.; Wang, C.; Hua, W.; Guo, Y.; Lu, G.; Gil, S.; Giroir-Fendler, A. Relationship between Catalytic Deactivation and Physicochemical Properties of LaMnO<sub>3</sub> Perovskite Catalyst during Catalytic Oxidation of Vinyl Chloride. *Appl. Catal. B Environ.* **2016**, *186*, 173–183. [[CrossRef](#)]
46. Díaz-Verde, Á.; Montilla-Verdú, S.; Torregrosa-Rivero, V.; Illán-Gómez, M.-J. Tailoring the Composition of Ba<sub>x</sub>BO<sub>3</sub> (B = Fe, Mn) Mixed Oxides as CO or Soot Oxidation Catalysts in Simulated GDI Engine Exhaust Conditions. *Molecules* **2023**, *28*, 3327. [[CrossRef](#)] [[PubMed](#)]

47. Najjar, H.; Lamonier, J.-F.; Mentré, O.; Giraudon, J.-M.; Batis, H. Optimization of the Combustion Synthesis towards Efficient  $\text{LaMnO}_{3+y}$  Catalysts in Methane Oxidation. *Appl. Catal. B Environ.* **2011**, *106*, 149–159. [[CrossRef](#)]
48. Lin, H.; Chen, D.; Liu, H.; Zou, X.; Chen, T. Effect of  $\text{MnO}_2$  Crystalline Structure on the Catalytic Oxidation of Formaldehyde. *Aerosol Air Qual. Res.* **2017**, *17*, 1011–1020. [[CrossRef](#)]
49. Buciuman, F.C.; Patcas, F.; Zsakó, J. TPR-Study of Substitution Effects on Reducibility and Oxidative Non-Stoichiometry of  $\text{La}_{0.8}\text{A}'_{0.2}\text{MnO}_{3+\delta}$  Perovskites. *J. Therm. Anal. Calorim.* **2000**, *61*, 819–825. [[CrossRef](#)]
50. Levasseur, B.; Kaliaguine, S. Effects of Iron and Cerium in  $\text{La}_{1-y}\text{Ce}_y\text{Co}_{1-x}\text{Fe}_x\text{O}_3$  Perovskites as Catalysts for VOC Oxidation. *Appl. Catal. B Environ.* **2009**, *88*, 305–314. [[CrossRef](#)]
51. Ulyanov, A.N.; Yu, S.-C.; Yang, D.-S. Mn-Site-Substituted Lanthanum Manganites: Destruction of Electron Pathway and Local Structure Effects on Curie Temperature. *J. Magn. Magn. Mater.* **2004**, *282*, 303–306. [[CrossRef](#)]
52. Díaz, V.A.; dos Santos, V.E.L.; Beltrán, H.H.; Huang, M.; Torregrosa, R.V.; Illán, G.M.J.; Cordoncillo, C.E. CO Oxidation Performance in GDI Engine Exhaust Conditions of  $\text{Ba}_x\text{Mn}_{0.7}\text{Cu}_{0.3}\text{O}_3$  ( $x = 1, 0.9, 0.8$  and  $0.7$ ) Perovskite Catalysts. In Proceedings of the 15th European Congress on Catalysis, Prague, Czech Republic, 27 August–1 September 2023.
53. Albaladejo-Fuentes, V.; Sánchez-Adsuar, M.-S.; Illán-Gómez, M.-J. Tolerance and Regeneration versus  $\text{SO}_2$  of  $\text{Ba}_{0.9}\text{A}_{0.1}\text{Ti}_{0.8}\text{Cu}_{0.2}\text{O}_3$  ( $A = \text{Sr}, \text{Ca}, \text{Mg}$ ) LNT Catalysts. *Appl. Catal. A Gen.* **2019**, *577*, 113–123. [[CrossRef](#)]
54. Fu, D.; Itoh, M.; Koshihara, S. Invariant Lattice Strain and Polarization in  $\text{BaTiO}_3$ - $\text{CaTiO}_3$  Ferroelectric Alloys. *J. Phys. Condens. Matter* **2010**, *22*, 052204. [[CrossRef](#)] [[PubMed](#)]
55. Su, B.; Button, T.W. Microstructure and Dielectric Properties of Mg-Doped Barium Strontium Titanate Ceramics. *J. Appl. Phys.* **2004**, *95*, 1382–1385. [[CrossRef](#)]
56. Chen, J.; Shen, M.; Wang, X.; Qi, G.; Wang, J.; Li, W. The Influence of Nonstoichiometry on  $\text{LaMnO}_3$  Perovskite for Catalytic NO Oxidation. *Appl. Catal. B Environ.* **2013**, *134–135*, 251–257. [[CrossRef](#)]
57. Levasseur, B.; Kaliaguine, S. Effect of the Rare Earth in the Perovskite-Type Mixed Oxides  $\text{AMnO}_3$  ( $A = \text{Y}, \text{La}, \text{Pr}, \text{Sm}, \text{Dy}$ ) as Catalysts in Methanol Oxidation. *J. Solid State Chem.* **2008**, *181*, 2953–2963. [[CrossRef](#)]
58. Peron, G.; Glisenti, A. Perovskites as Alternatives to Noble Metals in Automotive Exhaust Abatement: Activation of Oxygen on  $\text{LaCrO}_3$  and  $\text{LaMnO}_3$ . *Top. Catal.* **2019**, *62*, 244–251. [[CrossRef](#)]
59. Tien-Thao, N.; Alamdari, H.; Zahedi-Niaki, M.H.; Kaliaguine, S.  $\text{LaCo}_{1-x}\text{Cu}_x\text{O}_{3-\delta}$  Perovskite Catalysts for Higher Alcohol Synthesis. *Appl. Catal. A Gen.* **2006**, *311*, 204–212. [[CrossRef](#)]
60. Zhang, R.; Villanueva, A.; Alamdari, H.; Kaliaguine, S. Catalytic Reduction of NO by Propene over  $\text{LaCo}_{1-x}\text{Cu}_x\text{O}_3$  Perovskites Synthesized by Reactive Grinding. *Appl. Catal. B Environ.* **2006**, *64*, 220–233. [[CrossRef](#)]
61. Zhang, R.; Villanueva, A.; Alamdari, H.; Kaliaguine, S. SCR of NO by Propene over Nanoscale  $\text{LaMn}_{1-x}\text{Cu}_x\text{O}_3$  Perovskites. *Appl. Catal. A Gen.* **2006**, *307*, 85–97. [[CrossRef](#)]
62. Ashikaga, R.; Murata, K.; Ito, T.; Yamamoto, Y.; Arai, S.; Satsuma, A. Tuning the Oxygen Release Properties of  $\text{CeO}_2$ -Based Catalysts by Metal-Support Interactions for Improved Gasoline Soot Combustion. *Catal. Sci. Technol.* **2020**, *10*, 7177–7185. [[CrossRef](#)]
63. Hernández, W.Y.; Tsampas, M.N.; Zhao, C.; Boreave, A.; Bosselet, F.; Vernoux, P. La/Sr-Based Perovskites as Soot Oxidation Catalysts for Gasoline Particulate Filters. *Catal. Today* **2015**, *258*, 525–534. [[CrossRef](#)]
64. Konsolakis, M.; Carabineiro, S.A.C.; Marnellos, G.E.; Asad, M.F.; Soares, O.S.G.P.; Pereira, M.F.R.; Órfão, J.J.M.; Figueiredo, J.L. Volatile Organic Compounds Abatement over Copper-Based Catalysts: Effect of Support. *Inorg. Chim. Acta* **2017**, *455*, 473–482. [[CrossRef](#)]
65. Amadine, O.; Essamlali, Y.; Fihri, A.; Larzek, M.; Zahouily, M. Effect of Calcination Temperature on the Structure and Catalytic Performance of Copper–Ceria Mixed Oxide Catalysts in Phenol Hydroxylation. *RSC Adv.* **2017**, *7*, 12586–12597. [[CrossRef](#)]

**Disclaimer/Publisher’s Note:** The statements, opinions and data contained in all publications are solely those of the individual author(s) and contributor(s) and not of MDPI and/or the editor(s). MDPI and/or the editor(s) disclaim responsibility for any injury to people or property resulting from any ideas, methods, instructions or products referred to in the content.